Facilitating Breast Conserving Surgery Using Preoperative MRI

by

Jose Rincon

A thesis
presented to the University of Waterloo
in fulfillment of the
thesis requirement for the degree of
Master of Applied Science
in
Electrical and Computer Engineering

Waterloo, Ontario, Canada, 2018

Examining Committee Membership

The following served on the Examining Committee for this thesis. The decision of the Examining Committee is by majority vote.

Supervisor(s):	Dr. Oleg Michailovich Department of Electrical and Computer Engineering University of Waterloo
Internal Member:	Dr. Derek Wright Department of Electrical and Computer Engineering University of Waterloo
Internal Member:	Dr. George Freeman Department of Electrical and Computer Engineering University of Waterloo

I hereby declare that I am the sole author of this thesis. This is a true copy of the thesis, including any required final revisions, as accepted by my examiners.

I understand that my thesis may be made electronically available to the public.

Abstract

Breast cancer is currently considered the most widespread malignancy in women, which costs the lives of approximately 400,000 people annually worldwide. While extremely useful for early detection and diagnosis of breast disease, the application of Magnetic Resonance Imaging (MRI) to pre-operative planning of breast conservative surgeries is complicated due to the differences in the patient's posture at the time of imaging and surgery, respectively. Specifically, while MRI is standardly performed with patients positioned with their face down and their breast unrestricted and pendulous, breast surgeries normally require the patients to lie on their back, in which case the breast undergoes substantial deformations due to the effect of gravity. As a result of these deformations, pre-surgical MRI images frequently do not correspond with the actual anatomy of the breast at the time of surgery, which limits their applicability to pre-surgical planning. Accordingly, to overcome the above problem and make the MRI images align with the actual intra-surgical anatomy of the breast, the images need to be properly "warped" - a procedure that is known as prone-to-supine image registration. In many cases, this registration is carried out in two steps, prediction and correction. While the former involves bio-mechanical modeling used to describe the principal effect of tissue deformation, the latter refines the preceding results based on the image content. What is more important, however, is the fact that the accuracy of the correction step (and, hence, of the registration process as a whole) is strongly dependent on the accuracy of bio-mechanical modeling, which needs therefore be maximized as much as possible. Consequently, the fundamental objective of this research project has been the development of algorithmic solutions for reliable and accurate prediction. In particular, we propose an automatic detection of the location and geometry of the breast, and a breast image segmentation method to differentiate between adipose and dense tissue that is tractable, stable, and independent of initialization.

Acknowledgements

First of all, I want to thank Dr. Michailovich for the teachings and advice that he gave me during my studies at the University of Waterloo. Dr. Michailovich taught me to never stop learning and to always push myself towards excellence.

I would also like to thank Dr. Freeman and Dr. Wright. Thank you for your time, your feedback, and for all your help.

I would like to thank Amir, Côme, Daniel, George, Hossein, Laura, Ming, Olivier, Rinat, Rui, Wajiha, and the rest of my friends. Thank you so much for both academic and personal support that you gave me during my time at UW.

A special thanks to Anna-Maria for putting up with me and giving me all of her love and support.

Dedication

I would like to dedicate this thesis to my parents and my siblings. Thank you for loving me unconditionally and for never being more than a phone call away.

Table of Contents

List of Figures

List of Tables

List of Abbreviations

BCS Breast Conserving Surgery 38, 41

DCE-MRI Dynamic Contrast-Enhanced Magnetic Resonance Imaging 1

FEM Finite Element Modeling 11, 36, 38

GMM Gaussian Mixture Model 12, 21, 23, 30, 38, 41

MAP maximum *a posteriori* 9

MRI Magnetic Resonance Imaging iv, x, 1, 15–17, 29, 37

MSE Mean-Squared Error 10

RF Radio Frequency 2, 14

RMM Rician Mixture Model 16

SAD Sum of Absolute Differences 8

SNR Signal-to-Noise Ratio 1, 14, 21, 23, 24, 35, 38, 41

Chapter 1

Introduction

Breast cancer is the most widespread malignancy in women. Approximately 1.1 million cases of breast cancer are globally diagnosed each year, with the annual fatality costing 400,000 lives worldwide [4]. Since the introduction of screening mammography, morbidity from breast cancer has been reduced by more than 40 percent. However, situations in which the disease appears to be occult to mammography are still frequent. In such situations, as well as in cases of newly diagnosed breast cancer, a more powerful and accurate MRI examination is usually warranted.

Dynamic Contrast-Enhanced Magnetic Resonance Imaging (DCE-MRI) is currently considered the most sensitive method for non-invasive detection of breast cancer because it allows radiologists to see the location and shape of breast lesions. Moreover, by using MRI scans, surgical teams can improve surgical planning in order to achieve better surgical outcomes. However, accurate localization of breast lesions is a challenging task, as the posture of the patient at the time of imaging (facing down) differs considerably from the posture during surgery (facing up).

1.1 Application of MRI to breast conserving surgery

As mentioned above, breast MRI acquisition is standardly performed with subjects lying on their stomach, with their face turned down. This anatomical position is referred to as *prone* (see Subplot (a) of Figure 1.1). This position makes it possible to place the breast in close proximity of an array of MRI receiving antennas, which is done not only to increase the Signal-to-Noise Ratio (SNR), but also to reduce the frequency and phase contributions from tissues other than the breast. [5]. Moreover, the uncompressed and pendulous state of the breast helps to avoid tissue folding, thus further maximizing the accuracy of detection and localization of breast lesions.

During breast surgery, on the other hand, the same subjects will be normally lying on their backs, with their breast being largely deformed by the force of gravity. This anatomical position is called *supine* (see Subplot (b) of Figure 1.1). Although it is possible to acquire MRI images in this position as well, it is normally avoided in practice due to: a) low SNR,

b) the necessity to use surface Radio Frequency (RF) coils which may cause additional deformations, as well as c) the tendency of gravity-induced breast to obscure important diagnostic information.

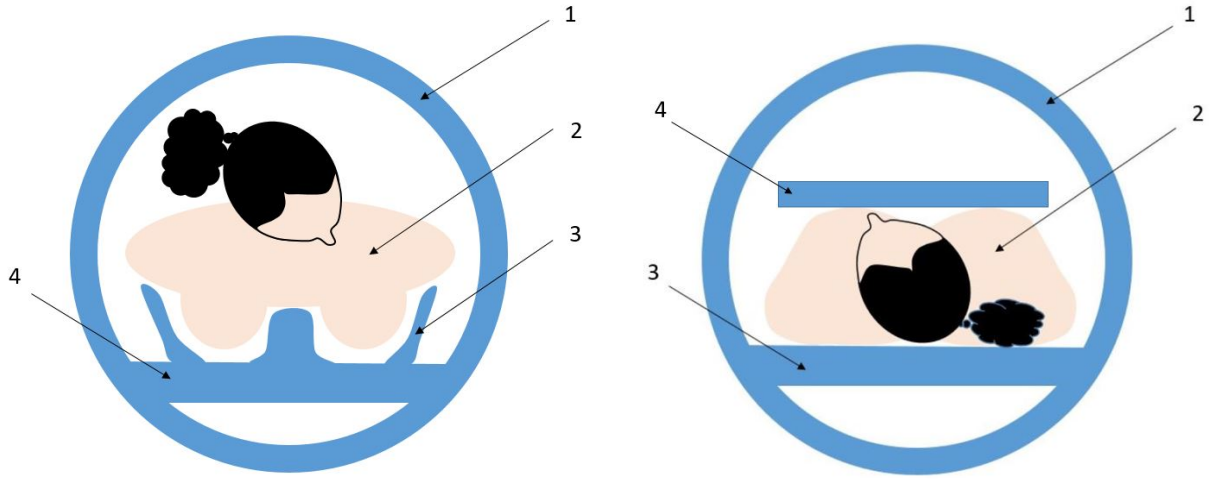

Figure 1.1: Subplot (a): Prone position. Subplot (b): Supine position.

In preparation for breast surgery, the breast lesions detected by prone MRI need to be correlated with their physical location in the supine position. This turns out to be a very non-trivial task for a number of reasons. First of all, visualization of 3-D medical imaging data is, in itself, an open-ended problem with effective solutions yet to be found. For example, some standard tools of 3-D visualization of MRI data are based on the so-called "three-panel view" (see Figure 1.2), which depicts three orthogonal cross-sections of an MRI volume under study. Second, as mentioned above, because of a large displacement of breast tissue due to the effect of gravity, the shapes of the breast in its prone and supine configurations are usually very different, which makes it quite challenging for the surgical team to correlate pre-operative MRI with the real anatomy. This difficulty, however, can be effectively alleviated by means of *prone-to-supine volumetric image registration* that consists on finding a deformation that can achieve this goal based on the mathematical tools of image processing. In this case, it is generally assumed that one is provided with both prone and supine MRI data (see Figure 1.3), where the former is used for the radiological management of breast disease, while the latter serves as a template to which the prone MRI scans (along with any relevant diagnostic information they may contain) are to be registered. Such registration allows the breast lesions detected by prone MRI to be "fused into" supine MRI scans, which agree much more closely with the configuration of the breast tissue at the time of surgery.

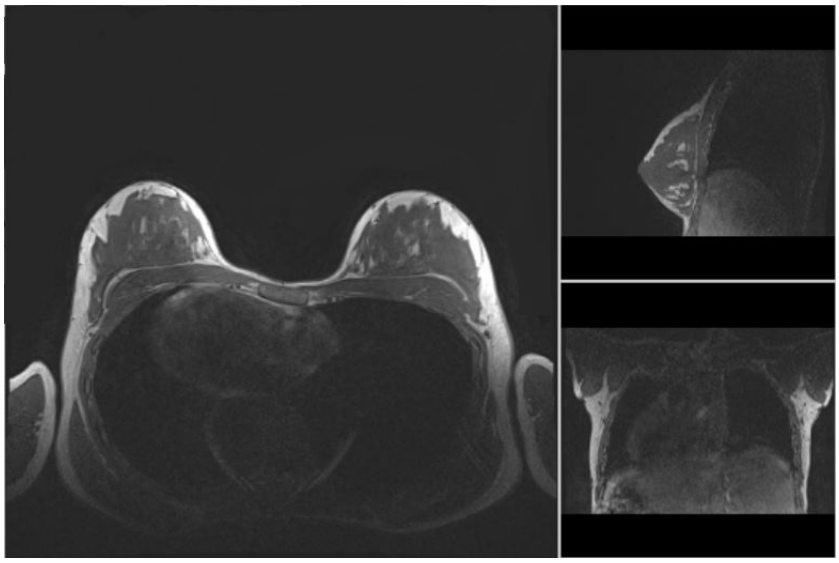

Figure 1.2: Typical axial, sagittal, and coronal visualization of breast MRI data.

1.2 Main contributions

Intensity-based image registration [6] is a standard procedure routinely used in medical imaging for the alignment of diagnostic scans that are known to be related to each other through geometric distortions. Such methods are known to be reasonably accurate for estimation of spatial deformations of small-to-medium amplitudes. Unfortunately with prone-to-supine registration of breast MRI scans, where typical deformations are sufficiently large to render most of the standard registration methods ineffective. In order to overcome this difficultly, a common solution is to "pre-warping" the prone images based on a *predicted deformation* provided through bio-mechanical modeling. When properly designed and executed, such "pre-warp" is capable of bringing the prone and supine images into much closer spatial agreement with each other. In this case, a residual (or correcting) deformation between the "pre-warped" prone and the original supine data is likely to have a relatively small amplitude, which in turn makes it possible to correct the predicted deformation by means of intensity-based image registration (see Figure 1.4). It is critical to emphasize that, since the success of the latter stage depends on how small the amplitude of the correcting deformation is, the accuracy of bio-mechanical modeling should be recognized as a critical part of the overall registration routine.

Typical application of bio-mechanical modeling requires one to associate each spatial position in an input image with a material element with predefined mechanical properties (such as density, elastic modulus, etc). Finding such an association entails two computational procedures, which are *breast extraction* (also known as whole-breast segmentation) and *breast segmentation*. In particular, the former refers to the procedure of finding an anatomical boundary of the breast, while the later involves the process of labeling the spatially bounded values into two classes of breast tissue, dense (e.g., fibro-glandular) and adipose tissue. The other possible classes of breast tissue may include skin and tumors, which have similar mechanical properties to adipose tissue and dense tissue respectively. For practical purposes

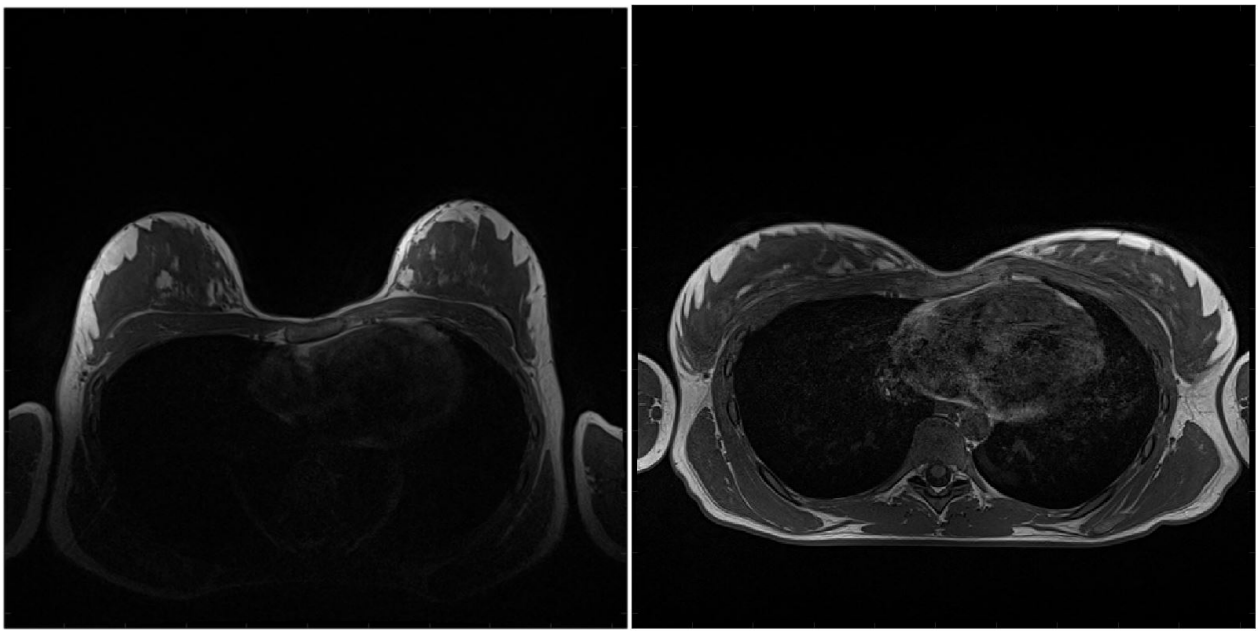

(a) (b)

Figure 1.3: Subplot (a): Image acquisition in prone position. Subplot (b): Image acquisition in supine position

these classes can be included into the principal classes. Unfortunately, neither of the above procedures is as simple as it might look at the first glance. The procedure of breast extraction requires finding a chest wall boundary, which is usually poorly discernible in MRI scans. As a result, in many cases, breast extraction is still performed manually, which is a very laborious process prone to human errors [7]. At the same time, the process of breast segmentation requires the estimation to be able to deal with signal dependent noise as well as variations in the image intensity due to the parasitic effect of the unshielded bias field [8]. Consequently, the existing methods of breast segmentation are rarely efficient computationally, and to guarantee convergence to solutions which are both accurate and unique.

Accordingly, this thesis pursued the goal of improving the quality of bio-mechanical modeling of breast deformation via the introduction of novel methods of breast extraction and breast segmentation. In particular, in this thesis we propose:

1. A novel method for fully automatic breast extraction, that requires neither initialization by a human operator nor further adjustments of numerical parameters.

2. A new method for automatic breast segmentation, which is capable of finding the optimal solution in an accurate and unique way.

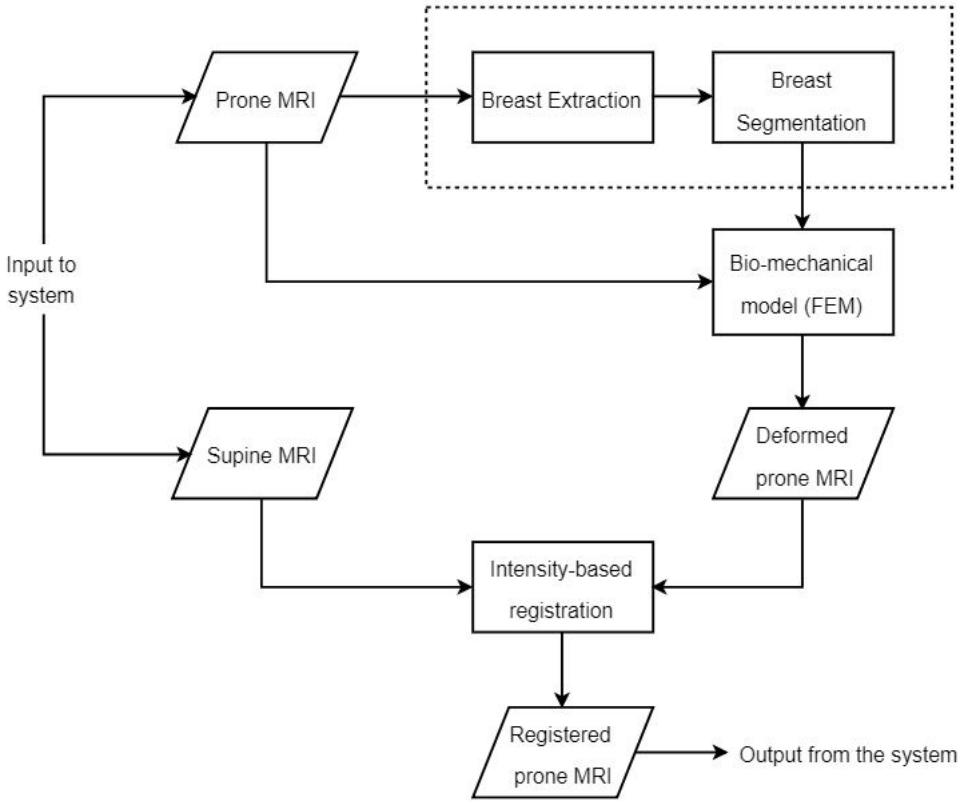

Figure 1.4: Flow diagram of the proposed prone-to-supine image registration method. Here the outlined (dashed) box indicates the main focus of this thesis.

1.3 Outline

The remainder of the thesis is organized as follows. Section 2 provides a literature review and presents some technical preliminaries necessary for the presentation of our results. Section 3 formulates the main research problems, and our solutions. Section 4 contains the results of performed numerical simulations as well as of our experiments with real-life data. The possible future extensions to this thesis are presented in Section 5.

Chapter 2

Literature review and technical preliminaries

2.1 Image registration

Given two real-valued images f and g defined over some (typically rectangular) domain $\Omega \subset \mathbb{R}^d$ (with $d = 2$ and $d = 3$ corresponding to the case of planar and volumetric images, respectively), the problem of image registration consists in finding a geometric transformation $\varphi : \Omega \to \Omega$ that is capable of bringing one of the two images (say, for example, f) into a close correspondence with the other. In particular, any image registration method relies on assuming the existence of an *optimal* spatial transformation $\varphi^* \in \Phi$, with Φ being the class of all possible deformations under consideration, such that $f \circ \varphi^*$ and g are properly *aligned*[1]. In practice, such optimal "warps" are not know in general, and hence, they are usually recovered using the provided imaging data. To this end, a standard approach to finding φ^* is to use a *distance measure* $\mathrm{Dist}(f \circ \varphi, g)$, whose global minimizer corresponds to the optimal deformation φ^*. Accordingly, the problem of image registration is normally formulated in the form of an optimization problem as given by

$$\begin{aligned} \text{minimize} \quad & \mathrm{Dist}(f \circ \varphi, g) \\ \text{subject to} \quad & \varphi \in \Phi \\ & \varphi(x_i) = y_i, \quad \forall i = 1, \ldots, N, \end{aligned} \tag{2.1}$$

where the equality constraints have been added for the sake of generality to include the cases when the user (radiologist) can manually indicate N fiducial landmarks x_i and y_i in the images f and g, respectively, which have to be in aligned. We note that the case of $N = 0$ corresponds to *itensity based image registration*, where f and g are registered based on their photometric values alone.

It goes without saying that different data and experimental settings give rise to various definitions of both Dist and Φ, each of which leads to a different registration algorithm. In

[1]The notation $f \circ \varphi$ stands for a composition of f and φ, suggesting $(f \circ \varphi)(x) = f(\varphi(x)), \forall x \in \Omega$.

what follows, we provide a number of typical examples, which are particularly relevant to our discussion.

2.1.1 Similarity measures

The choice of similarity measure Dist is arguably the most critical step in developing a useful image registration algorithm. There is a range of different definitions of Dist, which are designed to use the photometric, morphological, and/or statistical properties of f and g to various degrees. In many cases, the choice of Dist is defined by the contrast mechanism, underlying the formation of the data images. In particular, when f and g are known to be acquired using the same imaging modality, Dist is often chosen to be a standard metric of the form

$$\mathrm{Dist}(f \circ \varphi, g) = \int_{\Omega} |f(\varphi(x)) - g(x)|^p dx, \tag{2.2}$$

with $p \geq 1$. A particular choice of p usually depends on the expected behavior of the residual error $e(x) = f(\varphi(x)) - g(x)$. Thus, for instance, when the latter is expected to resemble white Gaussian noise, setting $p = 2$ is considered to be optimal in the sense of Maximum Likelihood (ML). Alternatively, when $e(x)$ is known to be spiky (thus allowing one to accommodate relatively large local deviations from the assumed model), setting $p = 1$ leads to a Dist in the form of a Sum of Absolute Differences (SAD). This similarity measure is known to be robust to occasional inconsistencies (outliers) in the data.

In the case when f and g are generated by two *different* imaging modalities (or, alternatively, by the same modality, yet using substantially different settings of its parameters), the images can no longer be expected to have close values at the same spatial coordinates. In this case, the definition of Dist needs to be properly adjusted to make it more sensitive to the morphological features of f and g, rather to their intensity values. A popular choice of such a measure is the *Negative Normalized Cross Correlation* that is given by

$$\mathrm{Dist}(f \circ \varphi, g) = -\frac{\int_{\Omega} \left(f(\varphi(x)) - \bar{f}\right)\left(g(x) - \bar{g}\right) dx}{\left[\int_{\Omega} |f(\varphi(x)) - \bar{f}|^2 dx\right]^{1/2} \left[\int_{\Omega} |g(x) - \bar{g}|^2 dx\right]^{1/2}}, \tag{2.3}$$

with $\bar{f}$ and $\bar{g}$ denoting the mean values of f and g, respectively. It is worthwhile noting that the above Dist is low bounded by the value of -1, which is attained when $f \circ \varphi$ and g happen to be identical.

Some additional and somewhat more advanced definitions of Dist that are routinely used in image registration are based on Mutual Information [9], its normalized version [10], and image gradients [11], to name a few.

2.1.2 Deformation models

Loosely put, a spatial deformation model is nothing else but a rule for changing the spatial coordinate x of each part of an image. The deformation models used in image registration can

be broadly characterized as being either *parametric* and *non-parametric*. In the former case, the final form of ϕ is governed by a set of its parameters θ. In this case, the optimization over φ can be replaced by an equivalent optimization over θ, which usually results in substantial improvements in both stability and computational efficiency of image registration. One of the most frequently used examples is the affine transformation given by [6]

$$\varphi(x) = A\,x + b, \tag{2.4}$$

where A is a non-singular, real $d \times d$ matrix and b is a spatial offset. In this case, θ consists of both A and b, in which case the total number of transformation parameters is equal to $d(d+1)$.

Depending on the choice of A, the above deformation model can be applied in a range of practically important situations. Thus, for example, restricting A to the set of orthogonal matrices gives rise to an *euclidean transformation*, in which case φ can only rotate and shift the content of f. Alternatively, an orthogonal A can be further multiplied by a diagonal matrix, which will add the possibility of scaling by incorporating the descriptive power of a deformation model. Most generally, applying φ given by (2.4) reproduces all possible rotations, shears, scalings and spatial shifts. It is its relatively high descriptive power in combination with its relatively low complexity which has made the affine model into the"model of choice" in many practical applications. One of the intrinsic properties of affine transformation is its ability to keep the zero curvature of straight lines.

As opposed to parametric models of φ, non-parametric models assume the latter to be a member of some predefined functional space Φ, the members of which do not admit representation in terms of model parameters. Instead, the membership of φ in Φ is usually defined via applying certain requirements on the norm of φ and/or of its higher-order derivatives. Some important examples of such non-parametric representations are based on the ideas of diffeomorphic topology preservation [12], linear elasticity [13], minimal bending energy [14], and others [15][16]. In such cases, it is typical to replace the *explicit* requirement $\varphi \in \Phi$ by requiring $\|\mathcal{D}(\varphi)\|$to be relatively small, which, for a proper choice of a differential operator $\mathcal{D}$ and norm $\|\cdot\|$, *implicitly* suggests the original constraint. Consequently, the methods of image registration using non-parametric φ are usually formulated in the form of an unconstrained optimization problem as given by

$$\min_{\varphi} \mathrm{Dist}(f \circ \varphi, g) + \lambda\,\|\mathcal{D}(\varphi)\|, \tag{2.5}$$

where $\lambda > 0$ is a user-defined regularization parameter. It is worthwhile noting that, from the viewpoint of statistical estimation, the solution of (2.5) can be shown to be optimal in the maximum *a posteriori* (MAP) sense, in which case the second term in the cost function above is related to a *prior* statistical model of φ [12].

When objects in the image are expected to have space dependent deformations, locally deformable registration models can be used. An example of these types of transformations is found in [17], where a free-from deformation based on cubic b-splines is utilized to align pre- and post-contrast images of the breast.

2.1.3 Optimization approaches

The cost function in in (2.1) can be minimized by various means, the choice of which is normally dictated by the definition of Dist. For cases where the distance metric is smooth (for instance when $p = 2$), gradient based optimization methods can be used [18]. However, when the distance metric is not smooth (for instance when $p = 1$), methods of non-smooth optimization can be used [19]. All the aforementioned methods are guaranteed to find a unique minimizer φ^*, if the $f(\varphi(x))$ term is convex. Unfortunately for many registration problems convexity does not hold. Nonetheless, for non-convex registration problems, the arduous process of finding a global minimizer of Dist can be replaced by the more practical task of finding a good local minima very close to φ^*. Obtaining a good final solution to non-convex optimization problems depends on initialization [18]. In the case of prone-to-supine image registration, the use of bio-mechanical models can help to find a good initial solution.

Several examples of image registration problems can be derived from the general image registration formula in (2.1) For instance, if Φ is set to be the space of cubic b-splines, $d = 0$, and the regularization constraint is the bending energy of a thin-plate metallic material [14], then registration problem is classified as a landmark-based approach. If in (2.1) normalized mutual information is used as the distance measure Dist, free-form deformations based on cubic b-splines as the deformation model Φ, the bending energy of a thin-plate of metallic material as a regularization constraint, and gradient descent as the optimization approach, we have the image registration algorithm presented by [17].

2.2 Modeling of anatomical deformations

The general image registration model from equation (2.1) can be applied to prone-to-supine breast MRI image registration. In this case, f and g represent the prone and supine MRI volumes, respectively. Assuming that both scans are acquired using the same MRI protocol, the Mean-Squared Error (MSE) as Dist (2.1) seems to be a logical choice. However, as mentioned previously, a direct application of intensity-based image registration is likely to produce a locally optimal solution of little practical value.

In order to solve the above problem current methods factorize φ into a composition of φ_L and φ_C, where φ_L is a transformation that predicts the large deformation of the breast, and φ_C is a correction of such prediction to account for residual misalignment. For finding φ_L it is conventional to use bio-mechanical modeling in conjunction with the numerical solution of corresponding differential equations [20], [7]. The residual deformation φ_C, on the other hand, can be subsequently found using a suitable image registration algorithm, such as [17].

2.2.1 Finite element model

The estimation of φ can be done within the framework of linear elasticity, which allows one to predict the displacement of breast tissue under the force of gravity. Once formulated,

the resulting differential equation is usually solved numerically by means of Finite Element Modeling (FEM)[21][22]. The governing equation of the linear elasticity model is [7]

$$\mathrm{M}\eta(\ddot{x}) + \mathrm{D}\eta(\dot{x}) + \mathrm{K}(\eta(x))\eta(x) = \mathrm{F}, \tag{2.6}$$

where $\eta(x)$ is the nodal displacement at location x, i.e., $\eta(x) = x - \varphi_L(x)$, M is the diagonalized lumped mass matrix, D is the diagonalized damping matrix, K is the stiffness matrix, and F are the forces acting on the body. The linear elasticity equations are solved numerically to find the nodal displacements $\eta(x)$ using the FEM, in which the body domain is discretized into the tetrahedral mesh to produce a nonlinear system of equations that is solved iteratively using, for example, Newton's method [23].

The estimate of φ_L can be used to "pre-warp" f towards g, followed by registration of $f \circ \varphi_L$ with the latter by means of intensity-based registration. The overall accuracy of the final transformation φ depends on the prediction step φ_L. By providing accurate information regarding the bio-mechanical model of the breast, φ_C will be more effective at predicting the deformation that brings f to close correspondence to g.

Hence, the main contribution of this thesis is to improve the accuracy of FEM through a more accurate description of the breast geometry. In this way we can improve the prediction step which in turn, when combined with the correction step, will improve the overall registration results.

2.3 Breast MRI segmentation

As mentioned previously, the state-of-the-art bio-mechanical model of prone-to-supine breast MRI deformations can be improved by utilizing a more accurate breast MRI segmentation algorithm. Breast MRI segmentation consist of labeling the spatial positions of the image into two classes, specifically, dense and adipose tissues. The other possible classes of breast tissues are skin and tumours which have similar mechanical properties to adipose and dense tissue, respectively. The technical preliminaries for breast MRI segmentation are provided in this section.

2.3.1 Segmentation of breast MRI scans

A general two-class image segmentation problem consists of partitioning the data domain Ω into two non-overlapping, constituent regions $\Omega_{in} \in \Omega$ and $\Omega_{out} \in \Omega$, where $\Omega = \Omega_{in} \cup \Omega_{out}$, $\Omega_{in} \cap \Omega_{out} = \emptyset$, which are associated with two different object classes represented by the data. The intensity value of the data, denoted by f, at coordinate x_i can be described by a random variable characterized with a probability density function (pdf) of the form

$$\mathrm{p}(f(x_i)|\theta) = u(x_i)\mathrm{p}(f(x_i)|\theta_{in}) + (1 - u(x_i))\mathrm{p}(f(x_i)|\theta_{out}), \tag{2.7}$$

where $\mathrm{p}(f(x_i)|\theta_{in})$ and $\mathrm{p}(f(x_i)|\theta_{out})$ are class-conditional pdf's, while $u(x_i)$ is an unknown indicator function that is defined as:

$$u(x_i) = \begin{cases} 1, & \text{if } x_i \in \Omega_{in} \\ 0, & \text{if } x_i \in \Omega_{out} \end{cases} \tag{2.8}$$

Given an image data $f = \{f(x)\}_{x\in\Omega}$, the ML-optimal value of the model parameters $\theta = \{\theta_{in}, \theta_{out}, u\}$ can be found via maximization of the likelihood function $L(\theta) := p(f = \{f(x)\}_{x\in\Omega}|\theta)$, namely

$$\hat{\theta}_{MLE} = \underset{\theta}{\operatorname{argmax}} \quad \mathrm{p}(f|\theta) = \underset{\theta}{\operatorname{argmax}} \quad \mathrm{L}(\theta). \tag{2.9}$$

Assuming the data values to be mutually independently allows rewriting $\mathrm{L}(\theta)$ in a simpler, factorized form as given by

$$\mathrm{L}(\theta) = \mathrm{p}(f|\theta) = \prod_{x_i\in\Omega} \mathrm{p}(f(x_i)|\theta), \tag{2.10}$$

where $\theta = \{\theta_{in}, \theta_{out}, u\}$ is the parameter of $\mathrm{p}(f(x_i)|\theta)$. Note that in practise it is more common to compute the estimate by minimizing the negative log-likelihood function $-\log \mathrm{L}(\theta)$ instead. Namely,

$$\hat{\theta}_{MLE} = \underset{\theta}{\operatorname{argmin}} \quad -\log \mathrm{L}(\theta) = \underset{\theta}{\operatorname{argmin}} \quad -\{\sum_{x_i\in\Omega} \log \mathrm{p}(f(x_i)|\theta)\}. \tag{2.11}$$

It should also be noted that, while the estimates of θ_{in} and θ_{out} may provide diagnostically important information on their own right, it is the function u that acts akin to a segmentation mask, thus dividing Ω into its anatomically meaningful sub-domains.

In what follows, we describe a number of standard finite mixture models that have been proposed in the past to segment breast MRI data.

2.3.2 Gaussian modeling for image segmentation

The simplest model that one can assume about the distribution of MRI data is that of a Gaussian Mixture Model (GMM) [24]

$$f_n(x_i) = f(x_i) + n(x_i), x_i \in \Omega, \tag{2.12}$$

where $f(x_i)$ is the noise-free breast MRI data, and $n(x_i)$ is a Gaussian additive noise at voxel x_i. In this case, the expected value of $f_n(x_i)$ is given by

$$\mathrm{E}\{f_n(x_i)\} = f(x_i) = \begin{cases} \mu_{in}, & \text{if } x_i \in \Omega_{in} \\ \mu_{out}, & \text{if } x_i \in \Omega_{out} \end{cases} \tag{2.13}$$

while the conditional densities of $f_n(x_i)$ are given by

$$\mathrm{p}(f_n(x_i)|\theta_{in}) = \frac{1}{\sqrt{2\pi\sigma_{in}^2}} \exp\left\{ - \frac{(f_n(x_i) - \mu_{in})^2}{2\sigma_{in}^2} \right\}, \tag{2.14}$$

with $\theta_{in} = \{\mu_{in}, \sigma_{in}\}$, and

$$\mathrm{p}(f_n(x_i)|\theta_{out}) = \frac{1}{\sqrt{2\pi\sigma_{out}^2}} \exp\left\{ - \frac{(f_n(x_i) - \mu_{out})^2}{2\sigma_{out}^2} \right\}, \tag{2.15}$$

with $\theta_{out} = \{\mu_{out}, \sigma_{out}\}$. For convenience we set $\theta = \{\theta_{in}, \theta_{out}\} = \{\mu_{in}, \sigma_{in}^2, \mu_{out}, \sigma_{out}^2\}$.

As usual, the ML-optimal values of θ are found via minimization of the negative log-likelihood functions $-\log \mathrm{L}(\theta)$, as given by (2.11). It should be noted that this optimization problem does not have a closed-form solution, thus calling for the use of methods of numerical optimization. Specifically, expectation-maximization (EM) is standardly used to solve numerical problems of this type [24].

Although important for numerous applications, the GMM model does not adhere naturally to the properties of MRI data, which is usually contaminated by non-Gaussian noise. In particular, a more accurate model in this case would be a mixture of Rician probability densities [8], which we introduce next.

2.3.3 Rician modeling for image segmentation

Noisy MRI data can be modeled by [8]:

$$f_n(x_i) = \sqrt{(f(x_i)\cos(\alpha) + n_R(x_i))^2 + (f(x_i)\sin(\alpha) + n_I(x_i))^2}, \tag{2.16}$$

where $f(x_i)\cos(\alpha)$ and $f(x_i)\sin(\alpha)$ are the projections of $f(x_i)$ onto the in-phase and quadrature directions of the receiving antenna, with α being the complex phase corresponding to $f(x_i)$. In this model, n_R and n_I denote two independent, zero-mean Gaussian random variables, which account for noise in the phase and quadrature receiver coils.

One can model such measurements using a Rician Mixture Model (RMM), with the conditional densities $\mathrm{p}(f_n(x_i)|\theta_{in})$ and $\mathrm{p}(f_n(x_i)|\theta_{out})$ given by [8]

$$\mathrm{p}(f_n(x_i)|\theta_{in}) = \frac{f_n(x_i)}{\sigma_{in}^2} \exp\left\{ - \frac{(f_n(x_i)^2 + \mu_{in}^2)}{2\sigma_{in}^2} \right\} I_0\left(\frac{f_n(x_i)\mu_{in}}{\sigma_{in}^2} \right), \tag{2.17}$$

with $\theta_{in} = \{\mu_{in}, \sigma_{in}\}$, and

$$\mathrm{p}(f_n(x_i)|\theta_{out}) = \frac{f_n(x_i)}{\sigma_{out}^2} \exp\left\{ - \frac{(f_n(x_i)^2 + \mu_{out}^2)}{2\sigma_{out}^2} \right\} I_0\left(\frac{f_n(x_i)\mu_{out}}{\sigma_{out}^2} \right), \tag{2.18}$$

with $\theta_{out} = \{\mu_{out}, \sigma_{out}\}$, and I_0 standing for the zeroth order modified Bessel function. An important property about the Rician distribution is that for voxels with high signal-to-noise ratio (SNR) it approximates to a Gaussian distribution [8]. In this case, the conditional densities of $f_n(x_i)$ follow (2.14) and (2.15) for the Ω_{in} and Ω_{out} regions, respectively.

2.3.4 Effect of MRI bias field on image segmentation

As mentioned previously, during breast MRI acquisition, the breast is placed inside a dedicated antenna to increase the SNR of MRI data. However, this makes the tissue closer to the RF antenna to have higher intensity values than the rest of the tissues in the breast MRI image. This effect can be modeled by a multiplicative bias field. Taking the multiplicative bias field into consideration, the conditional densities $\mathrm{p}(f_n(x_i)|\theta_{in}, b(x_i))$ and $\mathrm{p}(f_n(x_i)|\theta_{out}, b(x_i))$ should be properly modified as (see [8] for a detailed derivation)

$$\mathrm{p}(f_n(x_i)|\theta_{in}, b(x_i)) = \frac{f_n(x_i)}{\sigma_{in}^2} \exp\left\{ - \frac{b(x_i)(f_n(x_i)^2 + \mu_{in}^2)}{2\sigma_{in}^2} \right\} I_0\left(\frac{b(x_i) f_n(x_i) \mu_{in}}{\sigma_{in}^2} \right), \tag{2.19}$$

and

$$\mathrm{p}(f_n(x_i)|\theta_{out}, b(x_i)) = \frac{f_n(x_i)}{\sigma_{out}^2} \exp\left\{ - \frac{b(x_i)(f_n(x_i)^2 + \mu_{out}^2)}{2\sigma_{out}^2} \right\} I_0\left(\frac{b(x_i) f_n(x_i) \mu_{out}}{\sigma_{out}^2} \right), \tag{2.20}$$

where the effect of the bias field is represented by a positive multiplicative function $b : \Omega \to R_+$ that can be seen as a "correcting" image that point-wise multiplies the magnitude of the MRI data. In practice, b is known to be a smooth, slow-varying function of the spatial coordinate. For this reason, in this thesis we choose a low-order Bernstein polynomials for its parametric representation (see Appendix A for more details).

2.3.5 MRI segmentation in presence of a bias field

Similarly to the case of a two-class GMM, the probability density of $f_n(x_i)$ can be expressed by

$$\mathrm{p}(f_n(x_i)|\theta, b, u) = u(x_i)\mathrm{p}(f_n(x_i)|\theta_{in}, b(x_i)) + (1 - u(x_i))\mathrm{p}(f_n(x_i)|\theta_{out}, b(x_i)), \tag{2.21}$$

Subsequently, the problem of image segmentation can be formulated as the problem of minimization of the negative log-likelihood function $-\log L(\theta, b, u)$.

$$\begin{aligned} \underset{\theta,b,u}{\text{minimize}} \quad & -\log L(\theta, b, u) \\ \text{subject to} \quad & u(x_i) = \{0, 1\}. \end{aligned} \tag{2.22}$$

This optimization problem can be rewritten in its equivalent unconstrained form

$$\underset{\theta,b,u}{\text{minimize}} \quad -\log L(\theta, b, u) + I_{[0,1]}(u), \tag{2.23}$$

by using the indicator function given by:

$$I_{[0,1]}(u) = \begin{cases} 0, & \text{if } u \in [0, 1] \\ \infty, & \text{otherwise} \end{cases} \tag{2.24}$$

2.3.6 Incorporation of prior information

Many segmentation problems, including the segmentation of MRI data, are ill-posed in their nature, which often renders their solutions useless unless a proper regularization is employed. In particular, the fact that similar types of breast tissue tend to be anatomically connected allows one to consider the partition function to be of bounded variation [25], and therefore having a relatively low value of its total variation (TV) seminorm, given by

$$||u||_{TV} = \int_{x\in\Omega} |\nabla u(x)| dx. \tag{2.25}$$

Consequently, to avoid misclassification caused by over-segmentation due to the effect of bias fields and noise, one can regularize the problem at hand by supplementing the cost function by the TV term, thus leading to the problem of the form

$$(\theta_{ML}, b_{ML}, u_{ML}) = \underset{\theta,b,u}{\operatorname{argmin}} \quad L(\theta, b, u) + I_{[0,1]}(u) + \delta||u||_{TV}, \tag{2.26}$$

where $\delta > 0$ is a user-defined regularization parameter that weights the contributions of the total variation norm to the overall cost function. Needless to say, the cost function above is neither convex nor amenable to analytical treatment. Yet, in practice, it is usually straightforward to find a locally optimal solution by means of gradient-based optimization (subject, of course, to a proper relaxation of the non-differentiable TV term [26]).

A brief introduction to the problem of image registration was presented in this chapter. Moreover, the technical preliminaries for breast MRI image registration were given. In the next section we will examine our main contributions to the problem of prone-to-supine breast MRI registration.

Chapter 3

Problem formulation and main contribution

The main goal of this thesis is to improve the quality of the prone-to-supine breast MRI registration results. This can be done by improving the bio-mechanical model the of breast to achieve a more accurate prediction of φ_L which, in turn, will improve the final results after the correction step φ_c. In order to build the bio-mechanical model of the breast, one is required to find its anatomical boundary in the MRI data. The values enclosed by this boundary then must be labeled into the two classes of the breast, dense tissue (which also includes tumours), and adipose tissue (which also includes the skin). The more accurate the differentiation adipose and dense tissue in breast MRI data, the more accurate is the association of each spatial location of the data with a material element with predefined bio-mechanical properties.

3.1 Main contributions

There are two main contributions to this thesis. The first contribution, is an automatic method for detecting the voxels corresponding to breast tissue in MRI data. The second contribution consists of a conceptually novel approach for a two-class breast MRI segmentation under a Rician Mixture Model (RMM) assumption.

3.2 Whole-breast segmentation

In order to extract the breast volume from a prone MRI image, it is necessary to detect two boundaries: the boundary between air and the breast, and the boundary between the pectoralis muscle and the breast. Once these two boundaries have been detected, what lies within them is effectively considered as breast. The breast-muscle boundary detection is accomplished by using ITK-SNAP [27] in the reference method [7]. This software requires manual selection of initial contours for active contour evolution. Each slice of the MRI data

has to be processed in order to capture these regions. Alternatively, the breast boundaries can be manually traced with the same software.

Other methods, outside of the prone-to-supine breast MRI registration literature, have proposed automatic tools for breast boundary detection. For instance, in [28], Wang, et al. used a Hessian-based filter to enhance sheet-like structures that are similar to the breast-muscle boundary. The authors used a connected component filter based on the eigenvectors of the Hessian to remove structures that were misclassified as being part of the expected boundary. The authors point out that clutter can be removed and the broken pieces of the boundary can be connected by applying a connection cost filter, followed by a morphological closing filter with a $3 \times 3 \times 3$ kernel, both for dilation and erosion.

Another method is the one proposed by Wu et al. in [28]. In this method, the authors point out that muscle-breast boundary is the longest edge of each slice in sagittal view. They use a Canny edge detector, an anisotropic diffusion filter, and a bilateral filter to obtain three different images for each slice of the MRI data. The authors form a new image by including the edge features from the three filters. Then, they use dynamic program to traverse across all paths until the largest connected edge is found. The main drawback of this method is its computational complexity.

Breast MRI data contains information about many anatomical structures, not only breast, but also the pectoralis major, pectoralis minor, lungs, heart, liver, and other organs. The main goal of the whole-breast extraction method is to detect the voxels that belong to the breast domain from others. In the three images from Figure 3.1 we show the different compositions that breast tissue can have for three different subjects. For instance, subject number one, which is the left most image of Figure 3.1, has a breast composition high in fibroglandular tissue and very low in adipose tissue. Subject number two, which is located in the middle image of Figure 3.1, has a breast composition mostly dominated by adipose tissue. Subject number three, found in the right most image of Figure 3.1 is similar to the second subject, however, this subject's breast is much larger than the other two.

Figure 3.1: Examples of breast MRI from three different subjects.

These three subjects were chosen in this study to show how much breast tissue can vary from one subject to another, and to show that the proposed method works for a variety of cases.

In order to detect the voxels that correspond to breast tissue in MRI data, one is required to identify the boundaries that encompass breast tissue. Breast tissue is surrounded by two boundaries: the breast-air boundary, and the deep layer of the superficial fascia (see Figure 3.2).

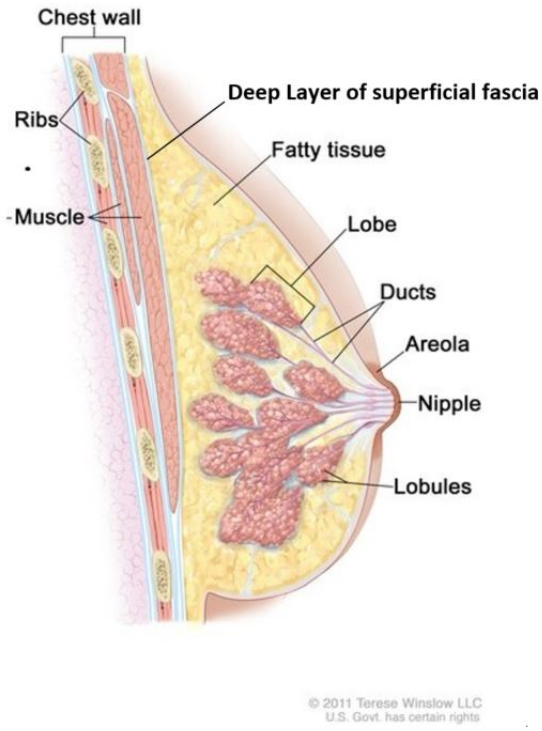

Figure 3.2: Anatomy of female breast.

In breast MRI, the breast-air boundary is the region between the background of MRI (air) and the most external fascia of breast (skin). The deep layer of the superficial fascia is a sheet-like structure between the pectoralis muscle and the adipose tissue right after the so-called retro-mammary fascia. The goal for this problem is to detect the boundary that separates breast from muscle, which is the deep layer of the superficial fascia. What makes this problem difficult is the fact that the typical resolution of MRI is often insufficient to effectively capture the deep layer of the superficial fascia. Thus, in MRI one only sees a transition from bright (adipose tissue) to dark (pectoralis). Depending on the type of breast tissue, one cannot guarantee that such a boundary will be captured by MRI. In this thesis, the proposed method for breast extraction is performed under the following assumptions.

1. It is possible to detect voxels that correspond to the deep layer of the superficial fascia in regions above the sternum. This is true because there is only skin and subcutaneous fat covering the sternum. Thus, regardless of the type of subject, there will always be two transitions. First, a transition from dark (air in MRI) to bright (skin and adipose tissue). And then, a transition from bright(adipose tissue) to dark (sternum).

2. There is a strong correlation between slices, i.e., the deep layer of the superficial fascia detected at one slice does not vary much with respect to the next slice.

3. The deep layer of the fascia can be recovered as the minimum path from a voxel, situated on top of the sternum and belonging to the deep layer of the superficial fascia, to another voxel, situated on the side of the torso and also belonging to the deep layer of the superficial fascia.

Based on the above assumptions, the proposed method for whole-breast extraction consists on the following steps (also shown in Figure 3.3).

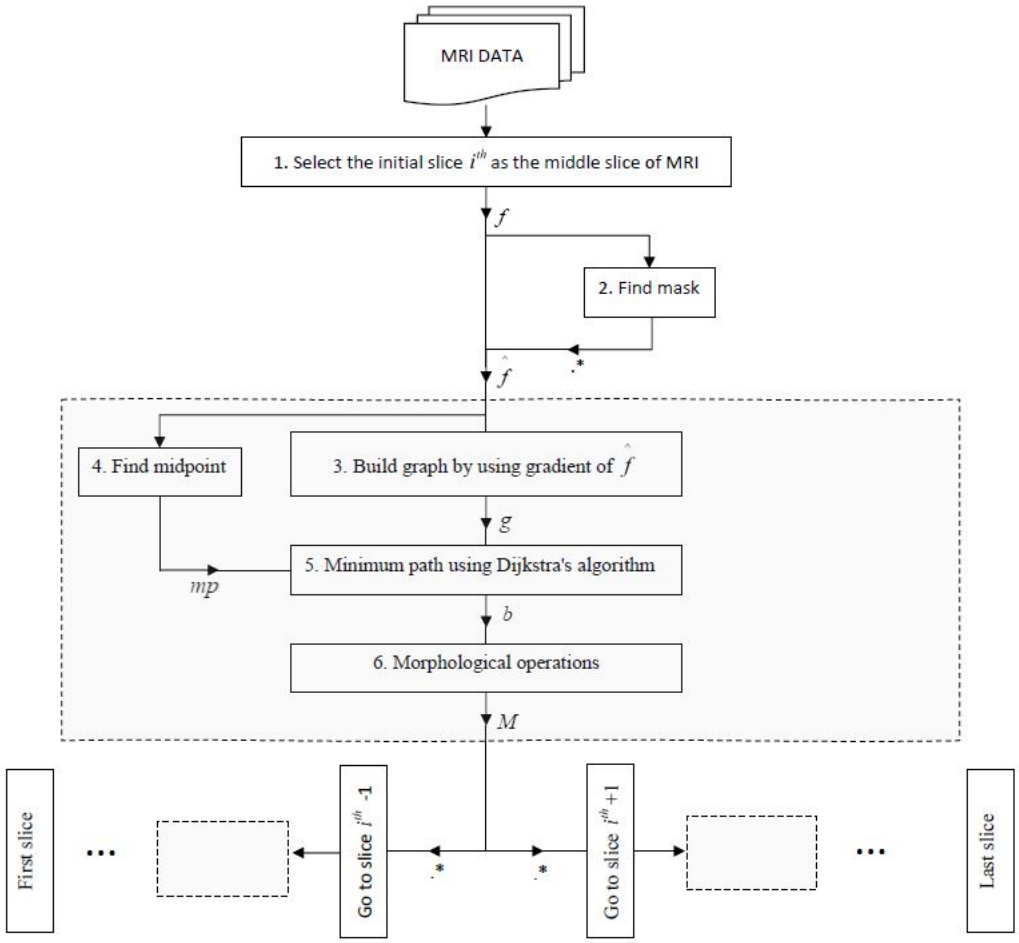

Figure 3.3: Flow diagram of the proposed algorithm for chest wall detection.

Step 1: The algorithm starts by selecting the slice in the middle of the sequence of MRI axial slices in order to have an axial view of the sternum in such slice. From the first assumption, one expects that detecting the deep layer of the superficial fascia will be relatively easy in this slice.

Step 2: This step consists on finding an adaptive threshold value to segment the breast and areas close to the breast from other organs in the initial slice. This generates a mask or binary image $M \in \{0, 1\}$, where values greater than or equal to the threshold are assigned a value of 1, and 0 otherwise. However, there is not a fixed value for this threshold that can

work for all cases. After several experiments, it was realized that this threshold even varies among slices. For this reason an adaptive threshold is used at each slice of the MRI image.

First one needs to find the sternum. This procedure is relatively easy. One can go about it by simply integrating over all the slices. The highest values located in the center of the image will correspond to the sternum. Since Dijkstra's algorithm will be used to find the deep layer of the superficial fascia, limiting the search scope reduces computational time. Therefore, one can crop all the image rows above a point located relatively higher but close to the sternum. After the image has been cropped, its histogram is computed. The threshold value for the hard segmentation of the region of interest is the value of the histogram's intensity interval that has the highest frequency. An kernel of size 3×3 is then utilized to compute the average value for the voxel situated in the middle of the kernel. If the averaging filter value is higher than the threshold, a value of 1 is assigned to the a given voxel; otherwise, a 0 value is assigned. This procedure effectively produces a binary mask that limits the search scope to the regions marked with a value of 1.

One can use the binary mask to element-wise multiply it with the initial breast MRI scan. Thus, all the voxels that belong to the breast are kept while discarding the background and most of the other organs that are not relevant. Note that organs of similar intensity values to the breast will still be present in the binary mask.

Step 3: This step consists in building a graph were each of the voxels of the image from step 2 are connected to its 8 nearest neighbors by links weighted by their gradient value. This is done because the boundary between the pectoralis and the breast is an edge. One knows that in T1 weighted MRI, the deep layer of the superficial fascia is found as a transition from high intensity (fat), to low intensity (pectoralis). Gradient values in the superfical fascia are expected to be high in absolute values. Therefore, a graph based on the inverse value of the gradient at each voxel is built. Each voxel is considered as a node, which is only connected to its 8 nearest neighbors. The weights are inversely proportional to the value of the gradient at each neighbor and voxel itself.

Step 4: Dijkstra's algorithm is used to find the minimum path between two points in the graph. The starting point of Dijkstra's algorithm is the point that belongs to the superficial fascia right below the sternum. This point can be easily detected from a slice where the sternum was previously detected by simply finding the gradient with respect to the y direction at that point.

Step 5: From the midpoint the minimum path to the left is found, and then to the right by using Dijkstra's algorithm. Since one roughly knows where the end of the pectoralis is on each side of the midpoint, this information is used as a stopping condition for Dijkstra's algorithm. After step 5, the deep layer of the superficial fascia is effectively recovered.

Step 6: Using the second assumption, can reduce the computational time of Dijkstra's algorithm by building the mask M of the next slice based on the detected boundary of the previous slice with morphological dilation. One can do this because one knows that the superfical fascia does not vary much in location between two consecutive slices. This allows one to have a smaller graph, thus speeding up computations.

This algorithm has been tested in the aforementioned three subjects, each of them with the most plausible tissue configurations. Figure 3.4 shows the results of the automatic chest wall

detection algorithm for subject number 1. It worth noting that for weak or even disconnected boundaries, the proposed algorithm still finds the correct boundary. This is due to the fact that Dijkstra's algorithm finds the minimum distance between the sternum and the end of the pectoralis, and if there is no clear boundary, the algorithm picks connection that minimizes the path.

One can do the same procedure for finding the upper boundary of the breast. However, this boundary of the breast is easier to find because of the high contrast between background and breast. An adaptive threshold based on the image histogram can be used to find this boundary. However, for higher accuracy purposes, Dijkstra's algorithm can be utilized as well.

The proposed method makes it is possible to detect the boundary between breast and muscle automatically, thus improving the reference method [7]. After the two boundaries that embed the breast have been found, one can assume that the remaining tissues in MRI only belong to the breast. In the next section, the problem of two class breast MRI image segmentation is discussed.

3.3 Segmentation of breast MRI scans

The reference method [7] assumes that the intensity values of each voxel from the MRI data is realization of a mixture of Gaussian random variables. In addition, the reference method uses a Markov Random Field to describe prior information, i.e., if one knows that a voxel belongs to the dense class, it is likely that its neighbors also belong to dense class. In the same way, if a voxel belongs to the adipose class, it is likely that its neighbors also belong to the adipose class. The solution to this segmentation problem is obtained by using the EM algorithm. A was pointed out in Section 2.3.3, a GMM is a suitable model for high SNR data. However, the reference method does not work well for data with low SNR. In the proposed method it is assumed instead that the intensity value for each voxel is a realization of a mixture of Rician random variables [8], given in Section 2.3.3. Under this consideration, it is possible to obtain more accurate segmentation results for creating a more precise bio-mechanical model of the breast.

3.3.1 Proposed method

The assumptions for the proposed method are the following:

1. It is assumed that the data has been preprocessed so that it only contains two classes: adipose and dense tissue. Please refer to Section 2.3.3 of this thesis for more details.

2. As mentioned previously, the bias field can be seen as a smooth multiplicative scalar field which can be parameterized by Bernstein's polynomials. For details about this implementation, please refer to Appendix A.

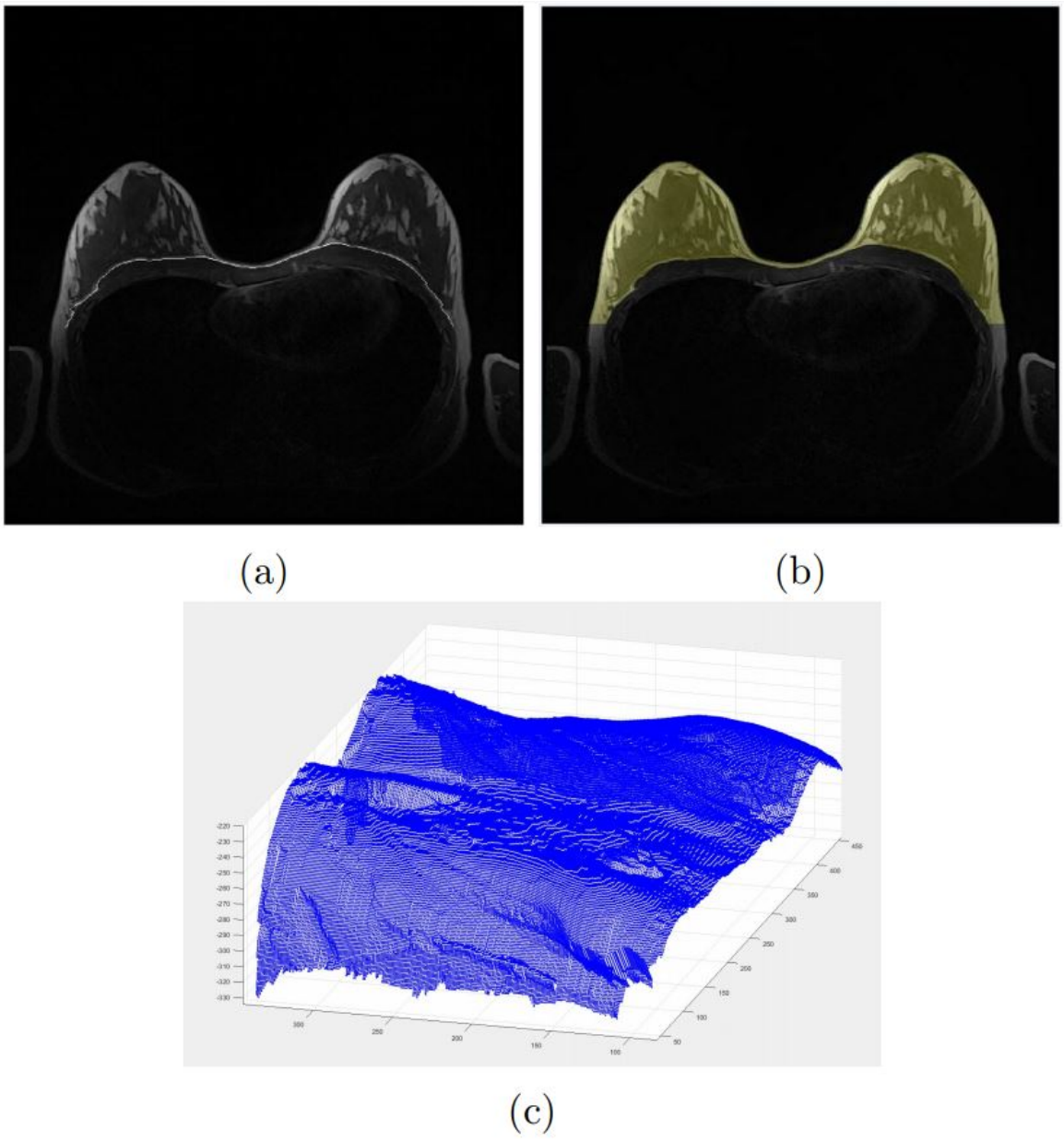

Figure 3.4: Subplot (a): Chest contour detected within one cross-sectional slice of an MRI volume; Subplot (b): Volumetric reconstruction of the chest wall.

Instead of assuming that the breast MRI data follows a GMM like in [7], or utilizing computationally expensive methods like [29], one can propose a method that effectively removes large outliers in Rician noise, and estimates the MRI bias field, thus, guaranteeing the "Gaussianity" of the noise of the resulting image and intensity homogeneity for the two tissue classes.

3.3.2 Processing of Rician noise

The elimination of the large outliers in Rician noise is outlined by the flow diagram in Figure 3.5.

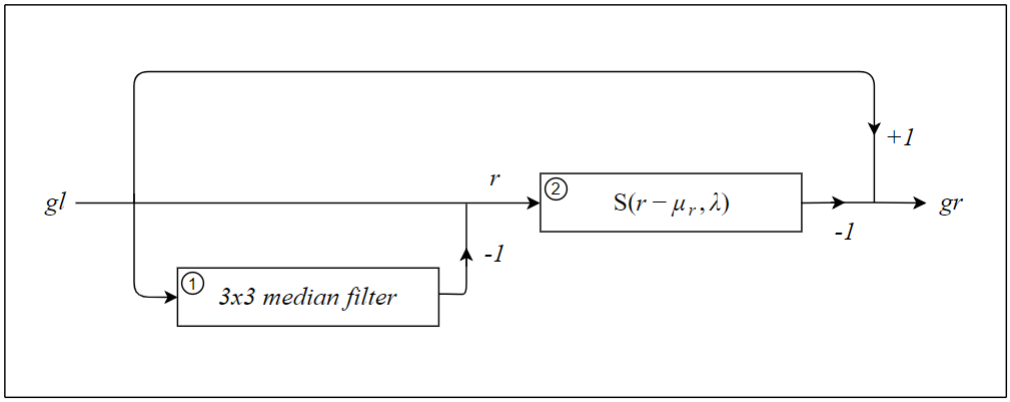

Figure 3.5: Flow diagram of the proposed method for Rician de-noising.

The voxels in the MRI data with low SNR are affected by Rician noise. In contrast, regions with high SNR, e.g., regions close to the dedicated antenna, are affected by Gaussian noise [8]. In the above diagram, gl denotes the magnitude MRI data which is assumed to be contaminated by both bias field and Rician noise. The first stage, given by block 1 in Figure 3.5, consists in smoothing the image with a 3×3 median filter; removing image outliers and replacing them with the median values of their 3×3 neighborhood. One obtains the residual data, denoted by r, by subtracting the filtered image in block 1 from the original image gl.

In order to detect the largest outliers of r, one can use a robust measure of deviation known as Median Absolute Deviation (MAD) because it is has superior efficiency for (non-Gaussian) data compared to that of the standard deviation [30]. The MAD of r, is given by

$$\lambda = \text{median}(|r - \mu_r|), \tag{3.1}$$

where μ_r is the median of r.

In block 2 of the flow diagram, the soft-thresholding operator is applied to $r - \mu_r$ with a threshold equal to λ. The soft-thresholding operator is defined by:

$$s(x, \lambda) = \begin{cases} x - \lambda \text{sign}(x), & \text{if} \quad |x| > \lambda \\ 0, & \text{otherwise} \end{cases} \tag{3.2}$$

where $\lambda > 0$ is a threshold value set so that the values of residual locations that fall in the interval $[-\lambda, \lambda]$ are set to 0. Therefore, the largest residuals are kept after block 2. The output of the flow diagram gr is the result of subtracting the largest residuals from the original image gl. In gr, one has removed the largest residuals in regions of low SNR; it is reasonable to assume that the residual noise now obeys a nearly Gaussian distribution. Figure 3.6 compares the histograms of Rician noise data before and after processing it to guarantee its "Gaussianity".

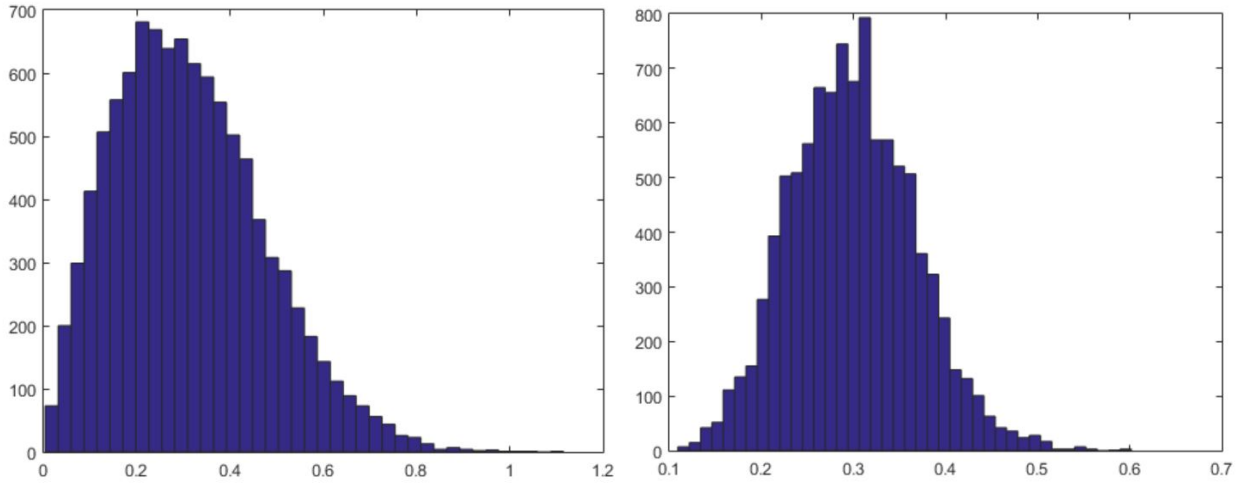

(a) (b)

Figure 3.6: Subplot (a): Histogram of Rician noise. Subplot (b): Histogram of noise after "Gaussianization"

3.3.3 Removal of bias field

Let D be a region of high SNR in a breast MRI data. Since it is known that D is less affected by noise, restricting the estimation of the bias field parameters to this regions can be expected to produce more accurate results. The underlying tissue in D is adipose tissue close to the MRI dedicated antenna. In this region the intensity values can be assumed to be a product of the bias field times the noise-free data:

$$F_n(x_i) = F(x_i)B(x_i), \tag{3.3}$$

where F_n is the measured data, F is the noise-free data, and B is the bias field at the x_i voxel. Taking a logarithmic transformation of F_n, one has:

$$f_n(x_i) = \log F_n(x_i) = f(x_i) + b(x_i), \tag{3.4}$$

where $f(x_i) = \log F(x_i)$, and $b(x_i) = \log B(x_i)$. By fitting the data points of f_n, for every x_i that one is certain that belongs to D, to a parametric function of Bernstein polynomials, one can estimate the total bias field and subtract it from f_n.

In order to find the locations x_i that belong to region D, the following segmentation algorithm is proposed:

- Compute the local variance of f_n with a Gaussian kernel with standard deviation equal to 2 and store it in data v_n.
- Select the voxels that have a local variance less than the median of v_n.

Due to the nature of the data, the proposed segmentation algorithm can only capture the voxels x_i that were not severely affected by noise and the bias field. Moreover, a very small set of voxels x_i that in reality did not belong to region D can get misclassified by the proposed segmentation algorithm. Therefore, it seems reasonable to formulate the estimation problem at hand as an ℓ_1 norm minimization problem which is known to be robust towards spurious outliers present in the data:

$$\underset{c}{\text{minimize}} \quad ||\Phi c - z||_1, \tag{3.5}$$

where the bias field $b = \Phi c \in \mathbb{R}^{\mathrm{n}}$ is given by Bernstein polynomials stored in a matrix $\Phi \in \mathbb{R}^{\mathrm{n}\times\mathrm{e}}$, and $c \in \mathbb{R}^{\mathrm{e}}$ are the coefficients, see Appendix A for more details. Moreover, $z \in \mathbb{R}^{\mathrm{n}}$ is the MRI data, after processing of Rician noise in section 3.3.2, and reshaped into a column vector. The problem in (3.5) can be rewritten in an equivalent constrained form as given by

$$\begin{aligned} \underset{c}{\text{minimize}} \quad & ||u - z||_1 \\ \text{subject to} \quad & \Phi c - u = 0. \end{aligned} \tag{3.6}$$

The augmented Lagrangian associated with this problem is:

$$L(u, c, p) = ||u - z||_1 + p^T(\Phi c - u) + (\delta/2)||u - z||_2^2, \tag{3.7}$$

where $p \in \mathbb{R}^{\mathrm{n}}$ is the dual variable, and $\delta > 0$ is the augmented Lagrangian penalty parameter [31]. The problem in (3.7) can be written by combining the linear and quadratic terms of the augmented Lagrangian, to result in

$$L(u, c, q) = ||u - z||_1 + (\delta/2)||\Phi c - u + q||_2^2, \tag{3.8}$$

where $q = \frac{p}{\delta}$. Using the Alternating Directions Method of Multipliers (ADMM) [31], the update of the primal variable c is as follows:

$$\begin{aligned} c_k^{t+1} &= \underset{u}{\text{argmin}} \; L_p(u, c, q) \\ &= \underset{c}{\text{argmin}} \quad ||u - z||_1 + (\delta/2)||\Phi c - u + q||_2^2 \\ &= \underset{c}{\text{argmin}} \quad (\delta/2)||\Phi c - u + q||_2^2 \\ &= \quad \Phi^{\dagger}(u^+ - q^t). \end{aligned} \tag{3.9}$$

The update of the primal variable u is as follows:

$$\begin{aligned} u_k^{t+1} &= \underset{u}{\operatorname{argmin}}\ L_p(u, c, q) \\ &= \underset{u}{\operatorname{argmin}} \quad ||u - z||_1 + (\delta/2)||\Phi c^{t+1} - u + q||_2^2. \end{aligned} \tag{3.10}$$

The problem in (3.10) admits a closed-form solution of the from:

$$u_k^{t+1} = \mathrm{S}(\Phi c^{t+1})_k + q_k + z_k\delta - z_k, \tag{3.11}$$

where S stands for the soft-thresholding operator defined in (3.2). The update in the dual variable is q is:

$$q_k^{t+1} = \Phi c^{t+1} + q - u^{t+1}. \tag{3.12}$$

Once the algorithm has converged to the optimal values u^* and c^*, the bias field is estimated as Φc^*.

3.3.4 Two-class image segmentation under the Gaussian Mixture Model

Now that the noise of the breast MRI data has been processed, one can assume that every intensity value of the MRI data f_n follows a mixture of two Gaussian random variables. The segmentation of a two-class breast MRI image f_n consist of partitioning the image domain Ω into two non-overlapping, constituent regions $\Omega_d \in \Omega$ and $\Omega_f \in \Omega$ corresponding to the dense and adipose regions, respectively. The segmentation problem can be tackled by minimizing the following cost function [32]

$$\begin{aligned} E(u, c, \mu_f, \mu_d) = \Bigg\{ &\sum_{x_i \in \Omega} \big(u(x_i)\lambda_1(f_n(x_i) - \mu_f - \Phi c(x_i))^2 \\ &+ (1 - u(x_i)\lambda_2(f_n(x_i) - \mu_d - \Phi c(x_i))^2\big) \\ &+ ||u||_{tv} + I_{[0,1]}(u)\Bigg\}, \end{aligned} \tag{3.13}$$

where $f_n(x_i)$ is the intensity value of the data at location x_i, and is assumed to follow a mixture of two Gaussian probability density functions $p(f_n(x_i)|\Omega_f)$ with mean μ_f, and $p(f_n(x_i)|\Omega_d)$ with mean μ_d. Moreover c are the coefficients of the bias field expressed by Bernstein polynomials, $\Phi c(x_i)$ is the bias field at location x_i, $\lambda_1 \in \mathbb{R}$, $\lambda_2 \in \mathbb{R}$, $u(x_i)$ was previously defined in (2.8), $I_{[0,1]}(u)$ is the indicator function from (2.24), and $||u||_{tv}$ is the total variation norm from (2.25).

Rewriting the original energy functional from (3.13) by using inner products, the image

segmentation problem can be expressed as:

$$\begin{aligned}\underset{u,c,\mu_f,\mu_d}{\text{minimize}} \quad & \left\langle u, \lambda_1 (f_n - \mu_f - \Phi c)^2 \right\rangle \\ & + \left\langle 1-u, \lambda_2 (f_n - \mu_d - \Phi c)^2 \right\rangle \\ & + ||u||_{TV} + I_{[0,1]}(u),\end{aligned} \tag{3.14}$$

where $<,>$ denotes the inner product operator, $u \in \mathbb{R}^{\mathrm{n}}$, $\mu_f \in \mathbb{R}^{\mathrm{n}}$ is vector with each component equal to the scalar value μ_f from (3.13), $\mu_d \in \mathbb{R}^{\mathrm{n}}$ is formed in the same way. Moreover, $\Phi \in \mathbb{R}^{\mathrm{n}\times\mathrm{e}}$, and $c \in \mathbb{R}^{\mathrm{e}}$. The problem in (3.14) can be rewritten in an equivalent constraint form given by

$$\begin{aligned}\underset{u,c,\mu_f,\mu_d}{\text{minimize}} \quad & \left\langle u, \lambda_1 (f_n - \mu_f - \Phi c)^2 \right\rangle \\ & + \left\langle 1-u, \lambda_2 (f_n - \mu_d - \Phi c)^2 \right\rangle \\ & + ||v||_{TV} + I_{[0,1]}(u) \\ \text{subject to} \quad & u - v = 0.\end{aligned} \tag{3.15}$$

The augmented Lagrangian associated with this problem is:

$$\begin{aligned}L(u,c,\mu_d,\mu_f,v,p) = & \left\langle u, \lambda_1 (f_n - \mu_f - \Phi c)^2 \right\rangle \\ & + \left\langle 1-u, \lambda_2 (f_n - \mu_d - \Phi c)^2 \right\rangle \\ & + ||v||_{TV} + I_{[0,1]}(u) \\ & + \frac{\delta}{2}||u - v + p||_2^2.\end{aligned} \tag{3.16}$$

Note that in (3.16) the linear and quadratic terms of the augmented Lagrangian have been already combined. the original problem in (3.14) This problem is solved by using ADMM with a total of four updates performed iteratively in the following order

$$\begin{aligned}u^{t+1} &:= \underset{u}{\text{argmin}} \quad L(u, v, c, \mu_d, \mu_f, p). \\ v^{t+1} &:= \underset{v}{\text{argmin}} \quad L(u^{t+1}, v, c, \mu_d, \mu_f, p). \\ c^{t+1} &:= \underset{c}{\text{argmin}} \quad L(u^{t+1}, v^{t+1}, c, \mu_d, \mu_f, p). \\ \mu_d^{t+1} &:= \underset{\mu_d}{\text{argmin}} \quad L(u^{t+1}, v^{t+1}, c^{t+1}, \mu_d, \mu_f, p). \\ \mu_f^{t+1} &:= \underset{\mu_f}{\text{argmin}} \quad L(u^{t+1}, v^{t+1}, c^{t+1}, \mu_d^{t+1}, \mu_f, p). \\ p^{t+1} &:= \quad p + u^{t+1} - v^{t+1}.\end{aligned} \tag{3.17}$$

The update of the variable u is as follows:

$$u^{t+1} = \underset{u}{\text{argmin}} \quad \left\langle u, (\lambda_1 - \lambda_2)(f_n - \mu_f - \Phi c)^2 \right\rangle + I_{[0,1]}(u) + \frac{\delta}{2}||u - v + p||_2^2. \tag{3.18}$$

The closed-form solution to this problem is given by

$$u^{t+1} = \Pi_{[0,1]}\left(v^t - p^t + \frac{(\lambda_2 - \lambda_1)(f_n - \mu_f - \Phi c)^2}{\delta^2} \right), \tag{3.19}$$

where $\Pi_{[0,1]}(x)$ is the orthogonal projection of x onto the interval $[0,1]$. The update of the primal variable v is as follows:

$$v^{t+1} = \underset{v}{\text{argmin}} \quad ||v||_{TV} + \frac{\delta}{2}||u - v + p||_2^2. \tag{3.20}$$

The problem is known as total-variation de-noising, and it can be solved by a variety of efficient methods of non-smooth optimization, such as the one detailed in [33]. Subsequently, the values of c, μ_d, and μ_f are updated by solving the following problem

$$\underset{\mu_f,\mu_d,c}{\text{minimize}} \quad \frac{1}{2}\big\langle (f_n - \mu_f - \Phi c)^2, u\big\rangle + \frac{1}{2}\big\langle (f_n - \mu_d - \Phi c)^2, u\big\rangle. \tag{3.21}$$

Solving the above problem can be facilitated through the following change of variables.

$$\begin{aligned} A_f &= [1 \quad 0 \quad \Phi] \\ A_d &= [0 \quad 1 \quad \Phi], \end{aligned} \tag{3.22}$$

where $1 \in \mathbb{R}^{n\times \mathrm{n}}$ and $0 \in \mathbb{R}^{n\times \mathrm{n}}$ are vectors with all of their components equal to 1 and 0, respectively. Another variable is θ is also introduced as

$$\theta = \begin{bmatrix} \mu_f \\ \mu_d \\ c \end{bmatrix}. \tag{3.23}$$

Using $A_f \in \mathbb{R}^{n\times 2\mathrm{n}+e}$, $A_d \in \mathbb{R}^{n\times 2\mathrm{n}+e}$, and $\theta \in \mathbb{R}^{2\mathrm{n}+e}$, one can re-write the problem stated in (3.21) as

$$\begin{aligned} \underset{\theta}{\text{minimize}} \quad & \frac{1}{2}\big|\big|W_{\sqrt{+}}\big(A_f\theta - f_n\big)\big|\big|_2^2 + \frac{1}{2}\big|\big|W_{\sqrt{-}}\big(A_d\theta - f_n\big)\big|\big|_2^2 \\ \text{subject to} \quad & e^T\theta = 0, \end{aligned} \tag{3.24}$$

where $W_{\sqrt{+}} = \mathrm{diag}(\sqrt{u}) \in \mathbb{R}^{n\times n}$, $W_{\sqrt{-}} = \mathrm{diag}(\sqrt{1-u}) \in \mathbb{R}^{n\times n}$. Moreover, $e = [1 \quad 1 \quad 0]^T \in \mathbb{R}^{2n+e}$, where each $1 \in \mathbb{R}^{1\times n}$ is a row vector with each component equal to 1, and $0 \in \mathbb{R}^{1\times e}$ is a vector row vector defined with each component equal to 0.

One cannot recover the parameters μ_f and μ_d because these values cannot be separated from the DC component of the bias field. However, with the constraint $e^T\theta = 0$, one is guaranteed to obtain a solution where $\mu_d \neq \mu_f$. The constraint $e^T\theta = 0$ was introduced in order to enforce our solution $\theta \in V_e^{\perp}$, where V_e is the *span* of e:

$$V_e = \big\{x \in \mathbb{R}^n | x = ue, \forall u \in \mathbb{R}\big\}. \tag{3.25}$$

In order to express the problem in a more compact form the following variables are introduced:

$$\begin{aligned} A_+ &\triangleq W_{\sqrt{+}}A_f\theta. \\ A_- &\triangleq W_{\sqrt{-}}A_d\theta. \\ y_+ &\triangleq W_{\sqrt{-}}f_n. \\ y_- &\triangleq W_{\sqrt{-}}f_n. \end{aligned} \tag{3.26}$$

The problem in (3.24) now can be re-written as:

$$\begin{aligned} \underset{\theta}{\text{minimize}} \quad & \frac{1}{2}\left(\left|\left|A_+\theta - y_+\right|\right|_2^2 + \left|\left|A_-\theta - y_-\right|\right|_2^2 \right) \\ \text{subject to} \quad & e^T\theta = 0. \end{aligned} \tag{3.27}$$

Recalling that $||Ax-b||_2^2 = (Ax-b)^T(Ax-b) = x^TA^TAx - 2b^TAx + b^Tb$, one can re-write (3.27) as:

$$\begin{aligned} \underset{\theta}{\text{minimize}} \quad & \frac{1}{2}(\theta^TA_+^TA_+\theta - 2y_+^TA_+\theta + y_+^Ty_+ + \theta^TA_-^TA_-\theta - 2y_-^TA_-\theta + y_-^Ty_-) \\ \text{subject to} \quad & e^T\theta = 0. \end{aligned} \tag{3.28}$$

Factoring the quadratic as well as the linear terms, and ignoring the constant terms of (3.28), one obtains:

$$\begin{aligned} \underset{\theta}{\text{minimize}} \quad & \frac{1}{2}\theta^TB\theta - 2\beta^T \\ \text{subject to} \quad & e^T\theta = 0, \end{aligned} \tag{3.29}$$

where $B = A_+^TA_+ + A_-^TA_-$, and $\beta = A_+^Ty_+ + A_-^Ty_-$. The Karush-Kuhn-Tucker (KKT) [18] conditions of the problem derived in (3.29) are:

$$B\theta^\star - \beta + \nu^\star e = 0, \quad e^T\theta^\star = 0, \tag{3.30}$$

where θ^*, ν^* are the primal and dual optimal points with zero duality gap that satisfy the KKT conditions [18], respectively. The equation above can be combined into a single system of linear equations of the form:

$$\begin{bmatrix} B & e \\ e^T & 0 \end{bmatrix} \begin{bmatrix} \theta^\star \\ \nu^\star \end{bmatrix} = \begin{bmatrix} \beta \\ 0 \end{bmatrix}. \tag{3.31}$$

From $\theta^\star$, one can recover μ_d^{t+1}, μ_f^{t+1}, and c^{t+1}. The update of the dual variable p from the Lagrangian in (3.16) is:

$$p^{t+1} = p^t + u^{t+1} - v^{t+1}. \tag{3.32}$$

Experimental results show that twenty iterations are usually sufficient for the convergence of the proposed segmentation procedure. Note that the only variable that one is interested in recovering is u, which tells the degree of membership of each voxel to the two regions in the MRI data, Ω_d and Ω_f.

In this chapter the novel methods for breast MRI extraction and segmentation of breast MRI scans were described. In the next chapter, the results of these algorithms for real breast MRI data will be shown.

Chapter 4

Experimental results

4.1 Simulation results

The proposed segmentation method was first tested using an artificially created 3D image. The 3D image was created by concatenating a series of the 2D Shepp-Logan phantom images [34] shown in Figure 4.1. As opposed to processing real data, the use of synthetic images allows one to quantify the performance of image segmentation under controllable conditions. The proposed two-class segmentation algorithm was executed for 20 iterations. The simulation results were compared against the two-class segmentation method used by the reference prone-to-supine image registration method in [7], which does not take into account the Rician nature noisy MRI data.

The FSL toolbox [1] was utilized for generating the comparison results of the reference method [7]. Just like the proposed algorithm, the reference method does estimate MRI bias field, and takes spatial dependencies into account. The results of this simulation study can be seen in Figure 4.1, where one can observe how the two-class segmentation method under a GMM is not suitable for segmenting noisy MRI data. While the breast MRI segmentation method used in [7] leaves behind a considerable amount of visible errors in segmentation, the proposed method is able to successfully achieve high accuracy in segmentation results.

4.2 Segmentation of real-life scans

Given the improvement achieved by the proposed method compared to the reference method [7] for simulated data, the next step is to test the novel two-class segmentation approach against the one utilized by the reference method for real breast MRI data. In this instance, real 3D breast MRI data acquired from the three subject samples in Figure 3.1 were segmented. The comparative results are shown in Figures 4.2 to 4.4.

Based on the artificial image results, it was expected that the reference method would yield relatively poor results when solving the two-class segmentation problem for real-life scans. However, both the proposed method and the reference method for breast MRI segmentation

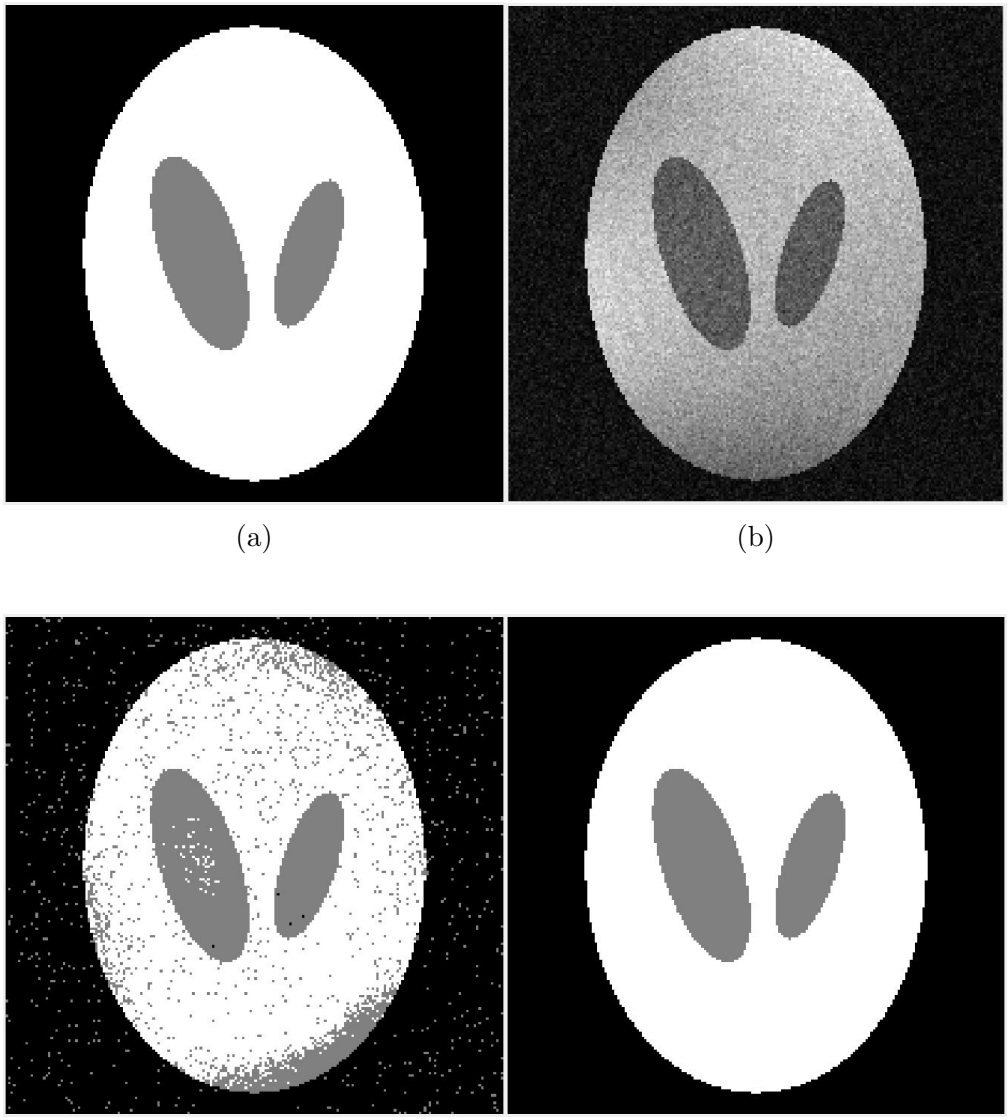

(a) (b)

(c) (d)

Figure 4.1: Subplot (a): Cross-sectional slice of a synthetic 3-D volume; Subplot (b): Same image contaminated by a bias field and measurement noise; Subplot (c): Segmentation results obtained using the reference method in [1]; Subplot (d): Segmentation results obtained with the proposed method.

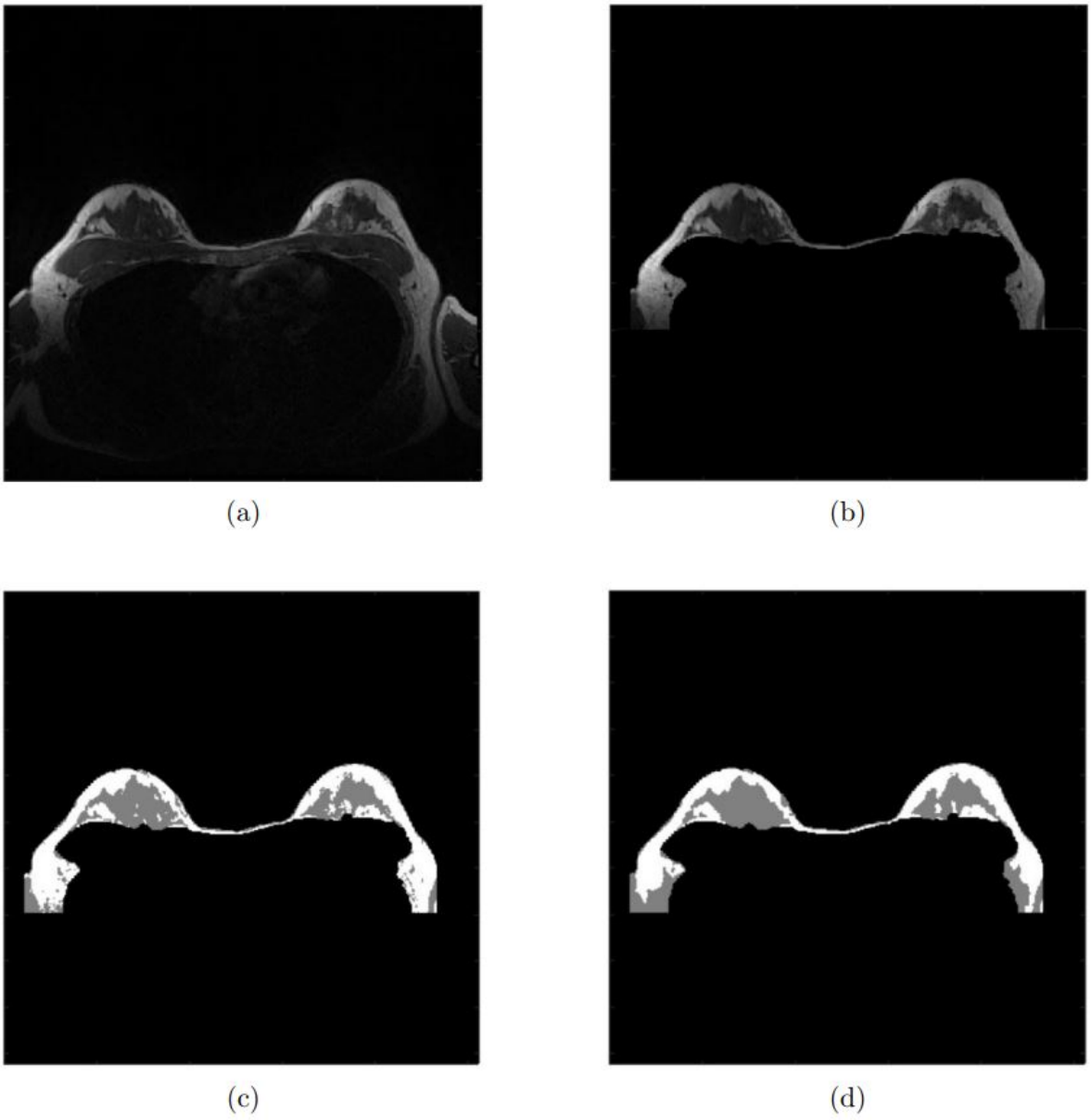

Figure 4.2: Subplot (a): Cross-sectional slice of Dataset 1; Subplot (b): Same slice shown after applying the procedure of whole-breast segmentation; Subplot (c): Segmentation results obtained using the reference method in [1]; Subplot (d): Segmentation results obtained with the proposed method.

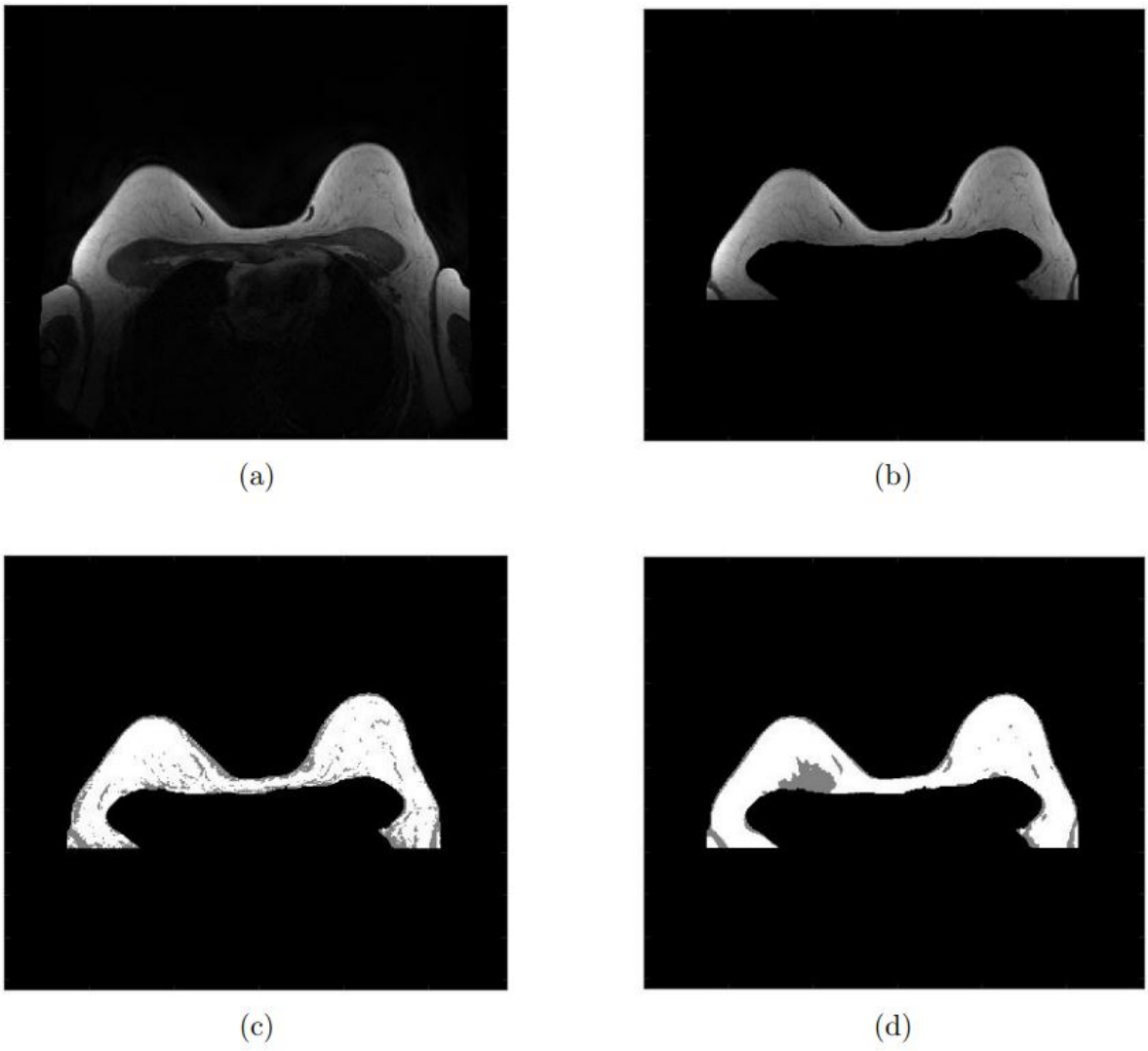

Figure 4.3: Subplot (a): Cross-sectional slice of Dataset 2; Subplot (b): Same slice shown after applying the procedure of whole-breast segmentation; Subplot (c): Segmentation results obtained using the reference method in [1]; Subplot (d): Segmentation results obtained with the proposed method.

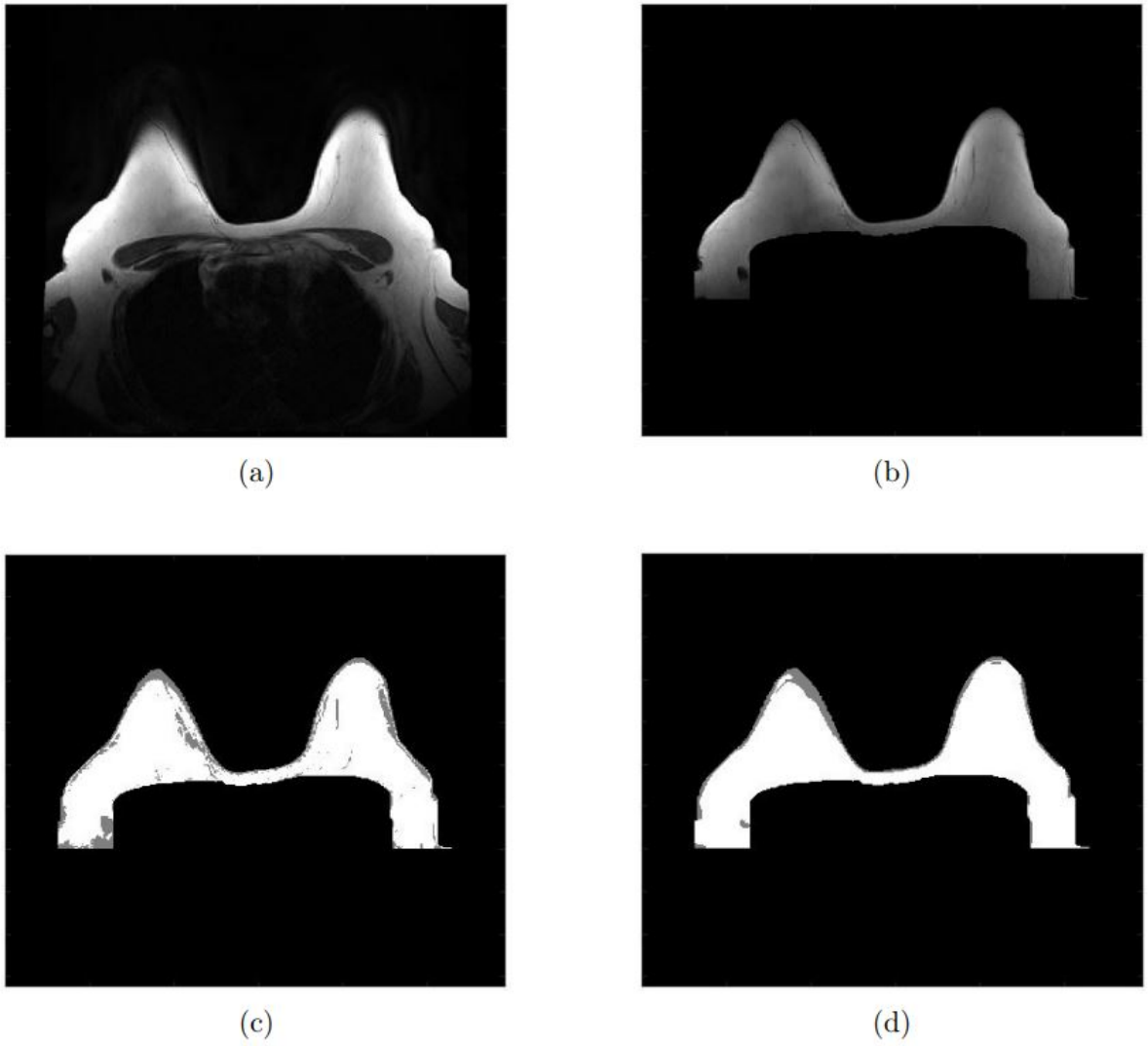

Figure 4.4: Subplot (a): Cross-sectional slice of Dataset 2; Subplot (b): Same slice shown after applying the procedure of whole-breast segmentation; Subplot (c): Segmentation results obtained using the reference method in [1]; Subplot (d): Segmentation results obtained with the proposed method.

			DSC	
Image	SNR (dB)	SSIM	MLE: GMM	Proposed Method
1	6.63	0.17	0.8654	0.9695
2	11.99	0.12	0.8582	0.9728
3	12.33	0.09	0.7924	0.9651
4	7.85	0.05	0.6943	0.9533
5	6.98	0.04	0.6522	0.9392
6	7.41	0.03	0.6469	0.9123

Table 4.1: Comparison of image segmentation methods for various noise levels. As one progresses from images 1 to 6, the quality of the image is affected more by noise. Since, SNR does not accurately reflect the perceived quality of an image, the SSIM metric is included as well [2]. The segmentation results of the reference and proposed method are compared with the Dice Similarity Coefficient (DCS) [3], where a value of 1 is attained for perfect segmentation results.

yielded comparable results. One can explain this phenomena because, as mentioned in Section 2.3.3, the intensity values of voxels with high SNR can be approximated by a mixture of Gaussian probability density functions. Since the breast is embedded in a dedicated antenna during image acquisition, the SNR in breast voxels is very high, and therefore, the Rician nature of noisy MRI data can be ignored. However, the proposed method provides a solution to the more general two-class MRI segmentation problem where images can be affected by Rician noise.

4.3 Prone-to-supine breast MRI registration

This section shows how the two proposed methods whole-breast extraction, and two-class breast breast MRI segmentation are incorporated as a pre-processing step for building the bio-mechanical model utilized in prone-to-supine breast MRI registration algorithm. In this section we also investigate whether it is possible to obtain similar or better results than those accomplished by the reference method [7]. The method by Han et al. [7], was chosen as the reference method because it uses a typical scheme for modeling the anatomical deformations in the prone-to-supine breast MRI registration: a prediction step φ_L using bio-mechanical modeling followed by a correction step φ_C based on image content. For these simulations the prone breast MRI data of the three subjects from Section 4.2 is used. The target images are the corresponding breast MRI images of the same three subjects acquired in supine position.

The assumptions for prone-to-supine registration are the following:

1. First, it is assumed that the surface given by the boundary between the ribs and the pectoralis is rigid. From human anatomy, it is known that muscle is attached to the ribs by tendons and that ribs are, in turn, attached to each other by ligaments [35].

2. It is assumed that the boundary between breast and muscle is also rigid. This assumption is valid because muscle has a relatively high theoretical Young's modulus of 9 kPa [36].

The prone-to-supine breast MRI registration method is accomplished following the steps in Figure 4.5.

Step 1: The prone breast MRI image is segmented, as described in Section 4.2, and each region is assigned a label based on the type of tissue it contains. All the locations in the adipose or dense regions are assigned a value of 1 or 2, respectively. The locations that do not belong to either adipose or dense regions are given a value of 0 and are not considered for building the bio-mechanical model of the breast. An additional class is introduced to simulate the torso, the static object that will serve as the support of the bio-mechanical model of the breast. All the locations below the pectoralis boundary are assumed to belong to this class, and are therefore given a value of 3.

Step 2: The toolbox, Iso2mesh [37], is utilized for FEM mesh generation over the domain that includes the three classes: adipose, dense, and torso (rigid object). This mesh is formed by nodes interconnected to produce the finite elements. In order to produce mesh with fewer number of nodes, it is advised to first build the mesh of the surface of the breast MRI data. Then smooth the surface using built-in Iso2mesh functions, and from this smoothed surface generate the finite elements of the volume. Doing this allows one to remove volume imperfections like islands or holes. This prevents the mesh generation method from creating an excessive amount of nodes to cover such topological defects.

Step 3: The bio-mechanical model of the breast is the generated. For each node of the mesh, the average of the intensity values of the closest spatial locations in the MRI image is computed using a $3 \times 3 \times 3$ kernel. The dominant class from within this neighborhood is then assigned to the node.

Step 4: All the nodes that were included in the torso must remain static during FEM. For this reason, these nodes are constraint with a zero motion Dirichlet boundary condition, before executing the FEM simulation.

Step 5: The anatomical deformation of the breast due to gravitational force is simulated using Matlab's PDE toolbox. This simulation displaces the locations of the nodes of the original mesh, producing a new deformed mesh.

Step 6: Based on the nodes of each mesh, a landmark-based image registration toolbox [38] is used to estimate the transformation φ_L that"pre-warps" the prone breast MRI image towards the supine breast MRI image.

Step 7: The residual misalignment is then corrected by the transformation φ_C, found using the image registration algorithm based on the Free-Form Deformation (FFD) method by Rueckert et al. [17]. This is done using NiftyReg [39], an open-source c_{++} image registration library.

To illustrate the steps of the prone-to-supine breast MRI registration algorithm, Figure 4.6 shows the deformation of the bio-mechanical model of the breast of subject number 1 due to gravity. Figure 4.7 shows the "pre-warped" image after applying φ_L, and the final

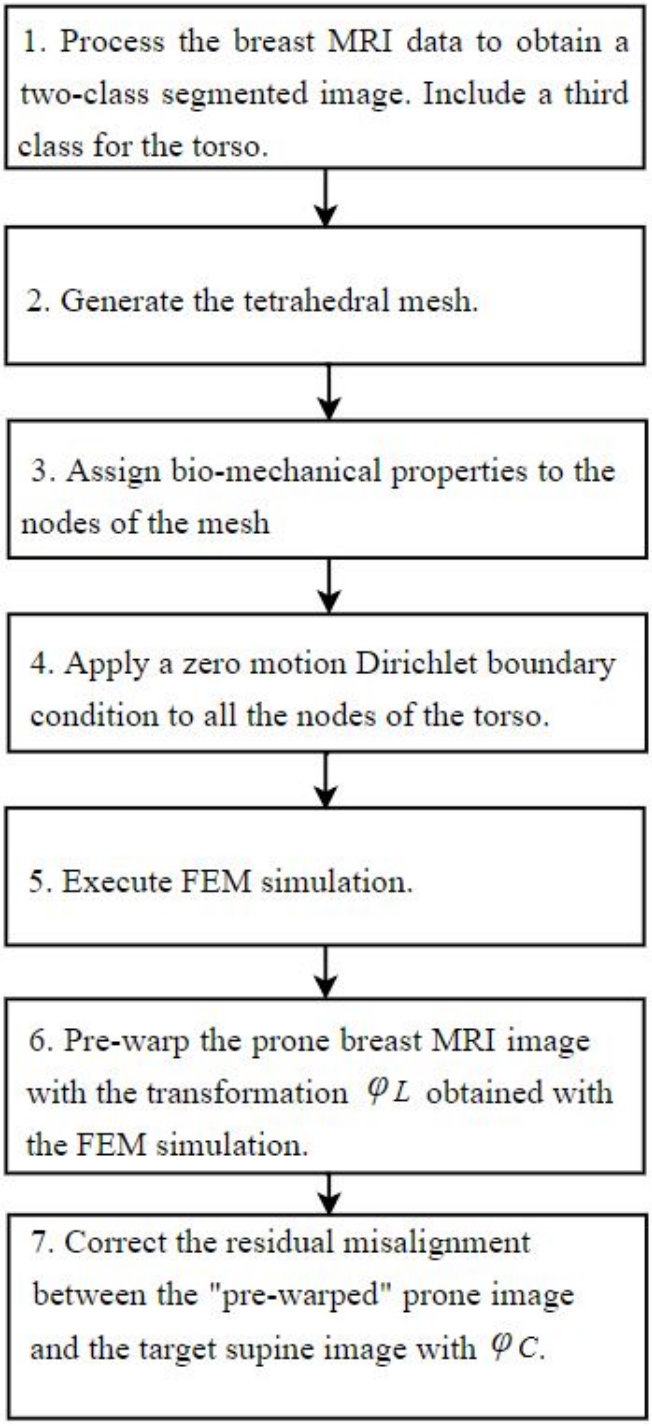

Figure 4.5: Block diagram of the proposed method for prone-to-supine breast MRI registration

Patient Number	Young's Modulus Fat (kPa)	Young's Modulus Dense (kPa)	Dice Coefficient with GMM Segmentation	Dice Coefficient with Proposed Method
1	500	650	0.8134	0.8201
2	500	600	0.7432	0.7324
3	690	690	0.3441	0.3525

Table 4.2: Quantitative assessment in terms of Dice coefficients

registration after applying the correction step φ_C for the same subject. Table 4.2 shows the prone-to-supine results of all three subjects.

It is worth mentioning that the supine breast MRI data of the subjects was acquired with their arms placed against either side of the torso. Unfortunately, since the bio-mechanical modeling of the breast did not include the arms, for subjects with large breasts there is not a constraint that stops the breast from sliding to the sides of the torso. Thus, for patients with large breasts the prediction step φ_L deforms the breast well beyond the actual deformation observed in the supine position, which results in very large residual misalignments that cannot be further recovered by the correction step φ_c.

In the reference method [7], the orientation of the gravitational vector is modified significantly in order to simulate the effect of having the subjects' arms containing the breasts laterally. Nonetheless, for subjects with small breasts the proposed registration method yielded results in the magnitude of those by the reference method [7], without modifying the orientation of the gravitational vector.

Subjects during Breast Conserving Surgery (BCS) usually have their arms extended laterally, perpendicularly to the torso, in an operating table. However, subjects are routinely asked to place their arms parallel to their torso during breast MRI acquisition. Even though one has the prone image and the supine image as a reference to check how accurate the registration results are, one cannot claim that the supine image captured from MRI represent the actual position of a subject on the operating table. This means that although previous studies have demonstrated successful prone-to-supine registration, further studies need to be carried in order to investigate the effect of the arms during bio-mechanical modeling.

The proposed two-class segmentation method does not significantly improve the segmentation results due to the high SNR of the MRI images used in the experiments. As mentioned previously, for high SNR values, the Rician Mixture Model of MRI is approximated by a GMM. Also, as long as the majority of the voxels are accurately classified as adipose or dense, the FEM method will yield approximately similar results. Nonetheless, it is good to note that thanks to the proposed automatic breast and muscle interconnection detection method, the pre-processing tasks for building the bio-mechanical model of the breast have been sped up.

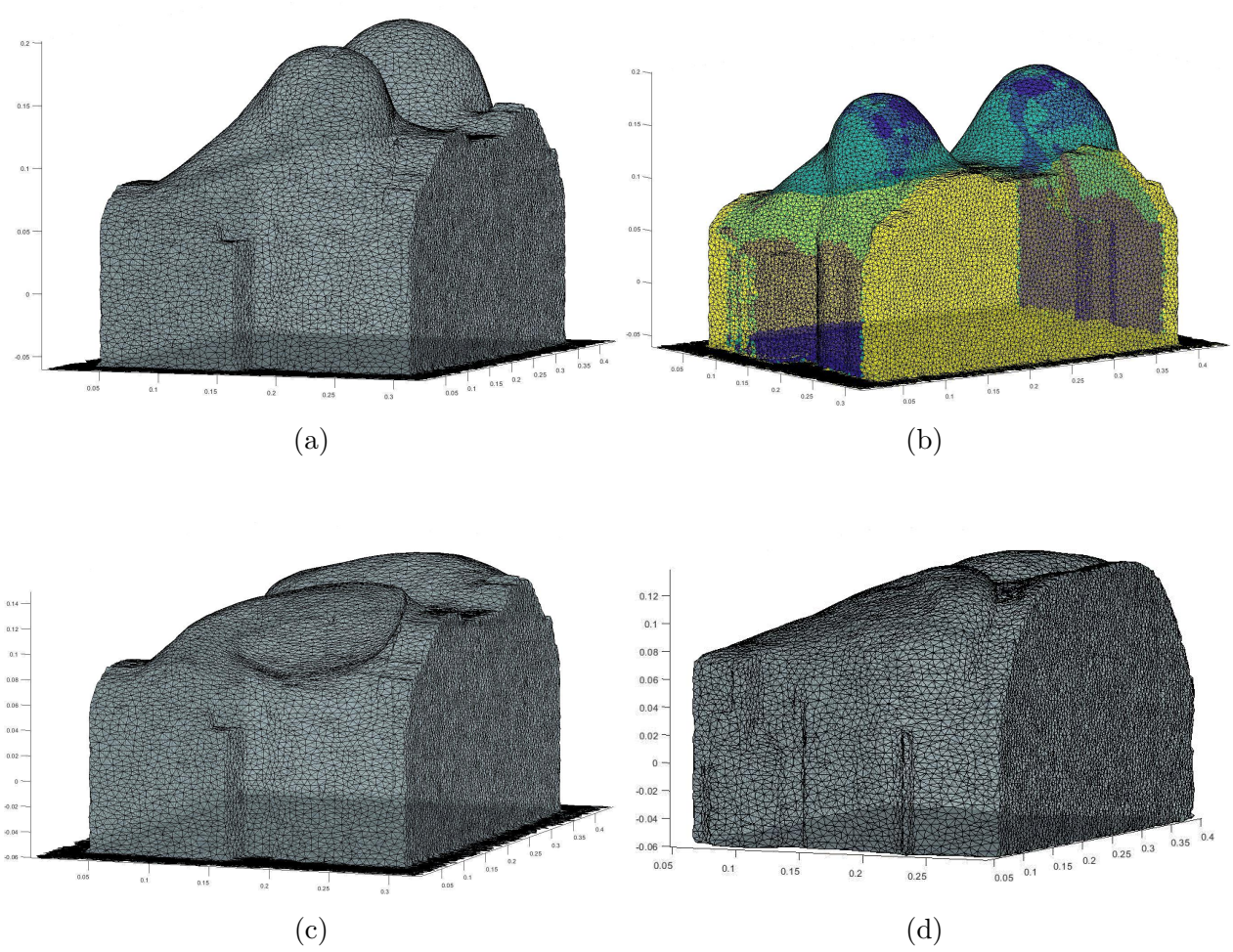

Figure 4.6: Subplot (a): Computational FEM mesh corresponding to a prone MRI volume; Subplot (b): Bio-mechanical properties of the mesh; Subplot (c): Ground truth mesh corresponding to a supine MRI volume; Subplot (d): Estimated mesh.

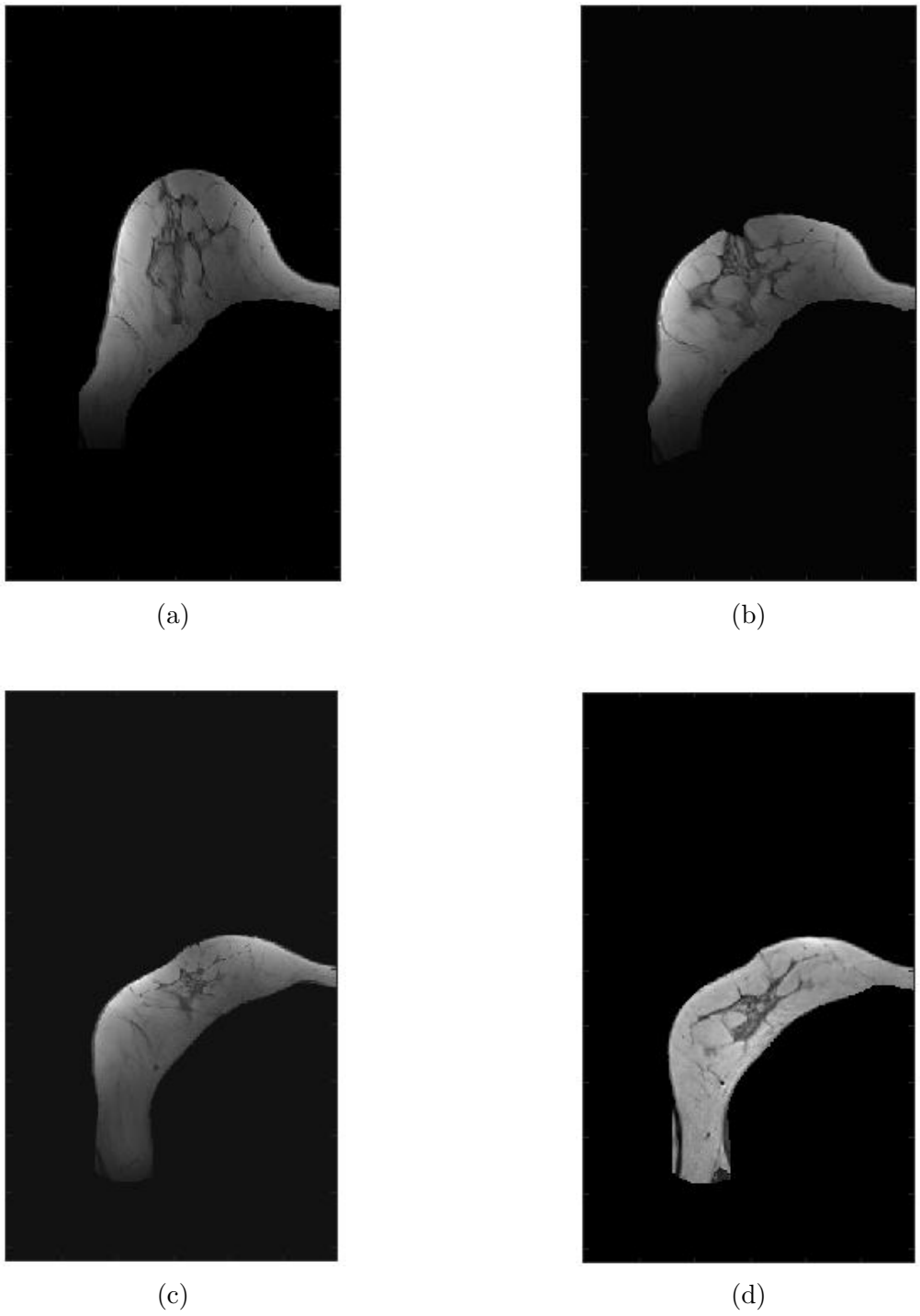

(a) (b)

(c) (d)

Figure 4.7: Subplot (a): Slice of prone MRI of dataset number 1; Subplot (b): Deformed prone MRI with φ_L; Subplot (c): Deformed prone MRI after applying the correction step φ_C; Subplot(d): Expected results based on MRI captured in supine position.

Chapter 5

Summary and Future Work

This thesis proposed an automatic whole-breast MRI extraction algorithm, and a novel two-class breast MRI segmentation method that can effectively differentiate between adipose and dense tissue in noisy MRI. The proposed two-class segmentation algorithm performed much better than the reference method [7] for noisy synthetic data. The better performance was achieved by considering the Rician nature of noise in MRI data. In contrast, for the real dataset utilized in this thesis, both algorithms yielded comparable results. The similar performance for the real dataset is due to the high SNR of the images. As was mentioned previously, the intensity values of data with high SNR, can be approximated by a GMM which is assumed in the reference method.

The proposed algorithms were included as the pre-processing step for the breast MRI prone-to-supine image registration. The prone-to-supine image registration algorithm was executed by estimating the effect of gravity with use of a bio-mechanical model, and then correcting the residual transformation by means of intensity-based image registration algorithm. The results achieved for subjects with small breasts were comparable to the current literature. However, future research efforts should focus on corner cases in which the interaction of the arms for subjects with large breast must be accounted. Nonetheless, this thesis is a step forward into a guidance system for BCS, and encourages future work into the development a method that can effectively predict the location of a patient's breast in supine position (position of the patient in the operating theater), based on the breast MRI data acquired in prone position.

APPENDIX

A. Implementation of MRI bias field

As was previously mentioned, MRI bias field can be seen as a slow-varying function of the spatial coordinate. For this reason, the bias field function can be described as a linear combination of Bernstein polynomials. For 3D MRI data, the bias field at location $x_i = (x_1, x_2, x_3)$ is modeled as the following tensor product:

$$b(x_1, x_2, x_3) = \sum_{l=0}^{n_A} \sum_{m=0}^{n_B} \sum_{n=0}^{n_C} \mathrm{P}_l^{n_A}(x_1) \mathrm{P}_m^{n_B}(x_2) \mathrm{P}_n^{n_C}(x_3) c_{l,m,n}, \tag{1}$$

where $c_{l,m,n}$ are the coefficients. The l^{th} Bernstein polynomial of degree n is defined by

$$\mathrm{P}_l^n(x) = \binom{n}{l} x^l (1-x)^{n-l}, \tag{2}$$

where $x \in [0, 1]$ is discretized by the number of voxels across the dimensions of the MRI data. Figure 1 shows the Bernstein polynomial up to the fifth degree inclusive. In practice the bias field can be stored as a vector $b \in \mathbb{R}^n$ which can be computed by:

$$\begin{aligned} b &= \Phi c, \text{ where} \\ \Phi \in \mathbb{R}^{\mathrm{dxe}} &= \mathrm{P}_A \otimes \mathrm{P}_B \otimes \mathrm{P}_C, \\ c &\in \mathbb{R}^{\mathrm{e}}, \end{aligned} \tag{3}$$

where c are the coefficients reshaped into a column vector of size $e = n_A n_B n_C$. Matrices P_A, P_B, and P_C contain the discretized Bernstein basis polynomials for the three dimensions of the data. Effectively, the l^{th} Bernstein polynomial of degree n is stored in the l^{th} column of matrices P_A, P_B, P_C. Moreover, Φ is a matrix resulting from applying the Kronecker product $\otimes$ between the aforementioned matrices.

Computing Φ results in an unnecessarily big matrix. However, thanks to the separability of polynomial basis, one does not need to compute this matrix. For a 2D MRI image, if one knows the coefficients $c \in \mathbb{R}^{n_A \times n_B}$, one can compute the bias field as:

$$b = \mathrm{P}_A c \mathrm{P}_B^T, \tag{4}$$

where c is reshaped to a column vector $c \in \mathbb{R}^{n_A n_B}$.

For the 3D case one can compute the bias field as:

$$b = \mathrm{P}_A^T c(\mathrm{P}_B \otimes \mathrm{P}_C), \tag{5}$$

where, c has been reshaped to $c \in \mathbb{R}^{l \times m \times n}$.

Alternatively, one can find the Bernstein basis polynomial coefficients given a known bias field. In 2D this computation is defined by:

$$c = \mathrm{P}_B^T b \mathrm{P}_A, \tag{6}$$

In 3D this computation is accomplished by:

$$c = \mathrm{P}_A b(\mathrm{P}_C \otimes \mathrm{P}_B)^T, \tag{7}$$

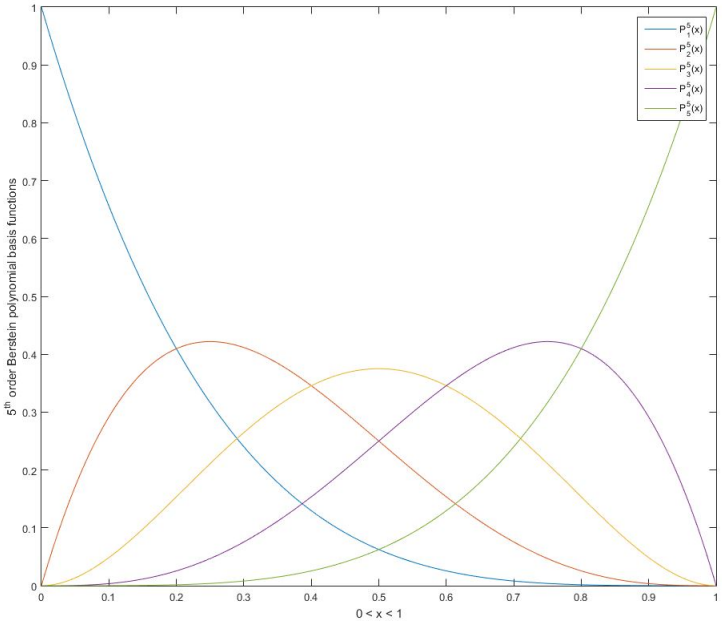

Figure 1: Fifth order Bernstein's polynomials basis functions.

More information about effective computation of the bias field exploiting basis separability please refer to the tensor decomposition content found in [40].

References

[1] S. M. Smith, M. Jenkinson, M. W. Woolrich, C. F. Beckmann, T. E. Behrens, H. Johansen-Berg, P. R. Bannister, M. De Luca, I. Drobnjak, D. E. Flitney *et al.*, "Advances in functional and structural MR image analysis and implementation as FSL," *Neuroimage*, vol. 23, pp. 208–219, 2004.

[2] Z. Wang, A. C. Bovik, H. R. Sheikh, and E. P. Simoncelli, "Image quality assessment: from error visibility to structural similarity," *IEEE transactions On Image Processing*, vol. 13, no. 4, pp. 600–612, 2004.

[3] L. R. Dice, "Measures of the amount of ecologic association between species," *Ecological Society of America*, vol. 26, no. 3, pp. 297–302, 1945.

[4] J. Ferlay, C. Héry, P. Autier, and R. Sankaranarayanan, "Global burden of breast cancer," *Breast Cancer Epidemiology*, pp. 1–19, 2010.

[5] R. Guillemaud and M. Brady, "Estimating the bias field of MR images," *IEEE Transactions on Medical Imaging*, vol. 16, no. 3, pp. 238–251, 1997.

[6] J. Modersitzki, *Numerical methods for image registration*. Oxford University Press on Demand, 2004.

[7] L. Han, J. H. Hipwell, B. Eiben, D. Barratt, M. Modat, S. Ourselin, and D. J. Hawkes, "A nonlinear biomechanical model based registration method for aligning prone and supine mr breast images," *IEEE Transactions on Medical Imaging*, vol. 33, no. 3, pp. 682–694, 2014.

[8] H. Gudbjartsson and S. Patz, "The Rician distribution of noisy MRI data," *Magnetic Resonance in Medicine*, vol. 34, no. 6, pp. 910–914, 1995.

[9] W. M. Wells, P. Viola, H. Atsumi, S. Nakajima, and R. Kikinis, "Multi-modal volume registration by maximization of mutual information," *Medical image analysis*, vol. 1, no. 1, pp. 35–51, 1996.

[10] C. Studholme, D. L. Hill, and D. J. Hawkes, "An overlap invariant entropy measure of 3D medical image alignment," *Pattern Recognition*, vol. 32, no. 1, pp. 71–86, 1999.

[11] J. P. Pluim, J. A. Maintz, and M. A. Viergever, "Image registration by maximization of combined mutual information and gradient information," in *International Conference*

on Medical Image Computing and Computer-Assisted Intervention. Springer, 2000, pp. 452–461.

[12] J. Ashburner, "A fast diffeomorphic image registration algorithm," *Neuroimage*, vol. 38, no. 1, pp. 95–113, 2007.

[13] C. Broit, "Optimal registration of deformed images," Ph.D. dissertation, University of Pennsylvania, 1981.

[14] C. R. Meyer, J. L. Boes, B. Kim, P. H. Bland, K. R. Zasadny, P. V. Kison, K. Koral, K. A. Frey, and R. L. Wahl, "Demonstration of accuracy and clinical versatility of mutual information for automatic multimodality image fusion using affine and thin-plate spline warped geometric deformations," *Medical Image Analysis*, vol. 1, no. 3, pp. 195–206, 1997.

[15] G. E. Christensen, R. D. Rabbitt, and M. I. Miller, "Deformable templates using large deformation kinematics," *IEEE transactions on Image Processing*, vol. 5, no. 10, pp. 1435–1447, 1996.

[16] K. P. Wilkie, "Mutual information based methods to localize image registration," Master's thesis, University of Waterloo, 2005.

[17] D. Rueckert, L. I. Sonoda, C. Hayes, D. L. Hill, M. O. Leach, and D. J. Hawkes, "Nonrigid registration using free-form deformations: application to breast MR images," *IEEE transactions on Medical Imaging*, vol. 18, no. 8, pp. 712–721, 1999.

[18] S. Boyd and L. Vandenberghe, *Convex optimization*. Cambridge university press, 2004.

[19] R. T. Rockafellar and R. J.-B. Wets, *Variational analysis*. Springer Science & Business Media, 2009, vol. 317.

[20] A. W. Lee, J. A. Schnabel, V. Rajagopal, P. M. Nielsen, and M. P. Nash, "Breast image registration by combining finite elements and free-form deformations," in *International Workshop on Digital Mammography*. Springer, 2010, pp. 736–743.

[21] A. Samani, J. Bishop, M. J. Yaffe, and D. B. Plewes, "Biomechanical 3-D finite element modeling of the human breast using mri data," *IEEE transactions on Medical Imaging*, vol. 20, no. 4, pp. 271–279, 2001.

[22] J. A. Schnabel, C. Tanner, A. D. Castellano-Smith, A. Degenhard, M. O. Leach, D. R. Hose, D. L. Hill, and D. J. Hawkes, "Validation of nonrigid image registration using finite-element methods: application to breast MR images," *IEEE Transactions on Medical Imaging*, vol. 22, no. 2, pp. 238–247, 2003.

[23] J. Fish and T. Belytschko, *A first course in finite elements*. John Wiley & Sons Limited, 2007.

[24] Y. Chen, M. R. Gupta, Y. Chen, and M. R. Gupta, "Em demystified: An expectation-maximization tutorial," *Electrical Engineering*, 2010.

[25] R. Acar and C. R. Vogel, "Analysis of bounded variation penalty methods for ill-posed problems," *Inverse Problems*, vol. 10, no. 6, p. 1217, 1994.

[26] D. C. Dobson and C. R. Vogel, "Convergence of an iterative method for total variation denoising," *SIAM Journal on Numerical Analysis*, vol. 34, no. 5, pp. 1779–1791, 1997.

[27] P. A. Yushkevich, J. Piven, H. C. Hazlett, R. G. Smith, S. Ho, J. C. Gee, and G. Gerig, "User-guided 3D active contour segmentation of anatomical structures: significantly improved efficiency and reliability," *Neuroimage*, vol. 31, no. 3, pp. 1116–1128, 2006.

[28] S. Wu, S. P. Weinstein, E. F. Conant, M. D. Schnall, and D. Kontos, "Automated chest wall line detection for whole-breast segmentation in sagittal breast MR images," *Medical Physics*, vol. 40, no. 4, 2013.

[29] S. Roy, A. Carass, P.-L. Bazin, S. Resnick, and J. L. Prince, "Consistent segmentation using a rician classifier," *Medical Image Analysis*, vol. 16, no. 2, pp. 524–535, 2012.

[30] C. Leys, C. Ley, O. Klein, P. Bernard, and L. Licata, "Detecting outliers: Do not use standard deviation around the mean, use absolute deviation around the median," *Journal of Experimental Social Psychology*, vol. 49, no. 4, pp. 764–766, 2013.

[31] S. Boyd, N. Parikh, E. Chu, B. Peleato, and J. Eckstein, "Distributed optimization and statistical learning via the alternating direction method of multipliers," *Foundations and Trends® in Machine Learning*, vol. 3, no. 1, pp. 1–122, 2011.

[32] B. Mory, R. Ardon, and J.-P. Thiran, "Variational segmentation using fuzzy region competition and local non-parametric probability density functions," in *Computer Vision, 2007. ICCV 2007. IEEE 11th International Conference*. IEEE, 2007, pp. 1–8.

[33] A. Chambolle, "An algorithm for total variation minimization and applications," *Journal of Mathematical imaging and vision*, vol. 20, no. 1, pp. 89–97, 2004.

[34] H. M. Gach, C. Tanase, and F. Boada, "2D & 3D shepp-logan phantom standards for MRI," in *Systems Engineering, 2008. ICSENG'08. 19th International Conference*. IEEE, 2008, pp. 521–526.

[35] D. U. Silverthorn, W. C. Ober, C. W. Garrison, A. C. Silverthorn, and B. R. Johnson, *Human physiology: an integrated approach*. Pearson/Benjamin Cummings San Francisco, CA, USA:, 2009.

[36] A. Gefen and B. Dilmoney, "Mechanics of the normal woman's breast," *Technology and Health Care*, vol. 15, no. 4, pp. 259–271, 2007.

[37] Q. Fang and D. Boas, "iso2mesh: A 3D surface and volumetric mesh generator for matlab/octave," 2010.

[38] D.-J. Kroon, "Non-rigid b-spline grid image registration toolbox," 2004.

[39] M. Modat, G. R. Ridgway, Z. A. Taylor, M. Lehmann, J. Barnes, D. J. Hawkes, N. C. Fox, and S. Ourselin, "Fast free-form deformation using graphics processing units," *Computer Methods and Programs in Biomedicine*, vol. 98, no. 3, pp. 278–284, 2010.

[40] T. G. Kolda and B. W. Bader, "Tensor decompositions and applications," *SIAM review*, vol. 51, no. 3, pp. 455–500, 2009.